JGR Planets

RESEARCH ARTICLE
10.1029/2021JE006903

Geological History of Southeastern Gorgonum Chaos, Mars: A Story of Water and Wind

David Haack[1], Solmaz Adeli[1], and Ernst Hauber[1]

[1]German Aerospace Center (DLR), Institute of Planetary Research, Berlin, Germany

Key Points:

- We produced a geological map of southeastern Gorgonum Chaos
- We find a succession from phyllosilicates to olivine in aeolian deposits
- The presence of water decreases over time

Correspondence to:
D. Haack,
david.haack@dlr.de

Citation:
Haack, D., Adeli, S., & Hauber, E. (2021). Geological history of southeastern Gorgonum Chaos, Mars: A story of water and wind. *Journal of Geophysical Research: Planets*, *126*, e2021JE006903. https://doi.org/10.1029/2021JE006903

Received 20 APR 2021
Accepted 20 AUG 2021

Abstract Gorgonum Chaos is part of the Eridania paleolake in Terra Sirenum and displays a number of prominent light-toned morphological features that bear a record of the regional climatic conditions throughout most of Martian history. Based on an intergrated analysis of orbital data, we mapped a 1,500 km^2 area in the southeast of Gorgonum Chaos. Morphologic, spectroscopic, and stratigraphic analyses were used to determine age and composition of the main geological units in the area. We identified four major geological units with decreasing content of hydrated minerals from the oldest to the youngest units, which were completely free of hydrated minerals. In the study area, phyllosilicate-rich Noachian units compose the majority of the basin floor. Deposits enriched with evaporites were formed around the Noachian/Hesperian transition and erosion created prominent inverted morphologies. Loess-like material without significant amounts of hydrated minerals was deposited until the late Hesperian. The youngest unit is an Amazonian layer free of hydrated minerals that originated from volcanic activities. This succession of minerals reflects the transition from more humid climatic conditions with the ability to sustain liquid water on the planet's surface during the Noachian to the hyper-arid Amazonian environment we observe currently on Mars.

Plain Language Summary Gorgonum Chaos is part of the Eridania basin, which is a former lake system located at the southern hemisphere of Mars. The landforms observed in this area and their variable brightness suggest dramatically changing climatic conditions during the history of Mars. In an area of 1,500 km^2 in size, we analyzed different landforms, their spectral characteristics, and their temporal sequences to determine the age and composition of the geological units. We found four major geologic units whose content of hydrated minerals decreased dramatically from oldest to youngest. The oldest unit with a high content of clay minerals is about 3.7 billion years old and formed the former lake bottom. This is followed by a younger unit with a mineral composition that indicates desiccation of the lake and erosion by wind. These, in turn, were largely covered by materials deposited by wind, which show very little evidence of liquid water. The last and youngest unit is volcanic in origin and completely devoid of minerals indicative of water. This succession of minerals reflects the evolution of the Martian surface, which was capable to sustain liquid water in the early stages of the planet and lost this ability during a drastic climate change.

1. Introduction

1.1. Background

During the geological evolution of Mars, the climatic conditions changed dramatically which resulted in a reduced sustainability of liquid surface water (Jakosky, 2021). This climate change may have taken place over an extended period of time and may have been episodically interrupted by aqueous phases. A transition from humid to arid climates most likely has been accompanied by a shift from chemical alkaline and neutral, clay forming environments to acidic, sulfate forming conditions (e.g., Bibring et al., 2006; Chaves et al., 2018; Hurowitz et al., 2010; Kaplan et al., 2016; Peretyazhko et al., 2017). This environmental transition should be reflected in the composition and in the stratigraphy of geological units.

Various studies showed that the highlands in Mars' southern hemisphere host a wide variety of ancient fluvial and lacustrine landforms, such as widespread valley networks (Alemanno et al., 2018; Hynek et al., 2010) and large basins that hosted paleolakes (e.g., Davila et al., 2011; Pajola et al., 2016; Wray et al., 2011). The morphological and mineralogical characteristics of the units related to these landforms and the associated aqueous processes are profound records of past climatic conditions on Mars. Although the highlands are

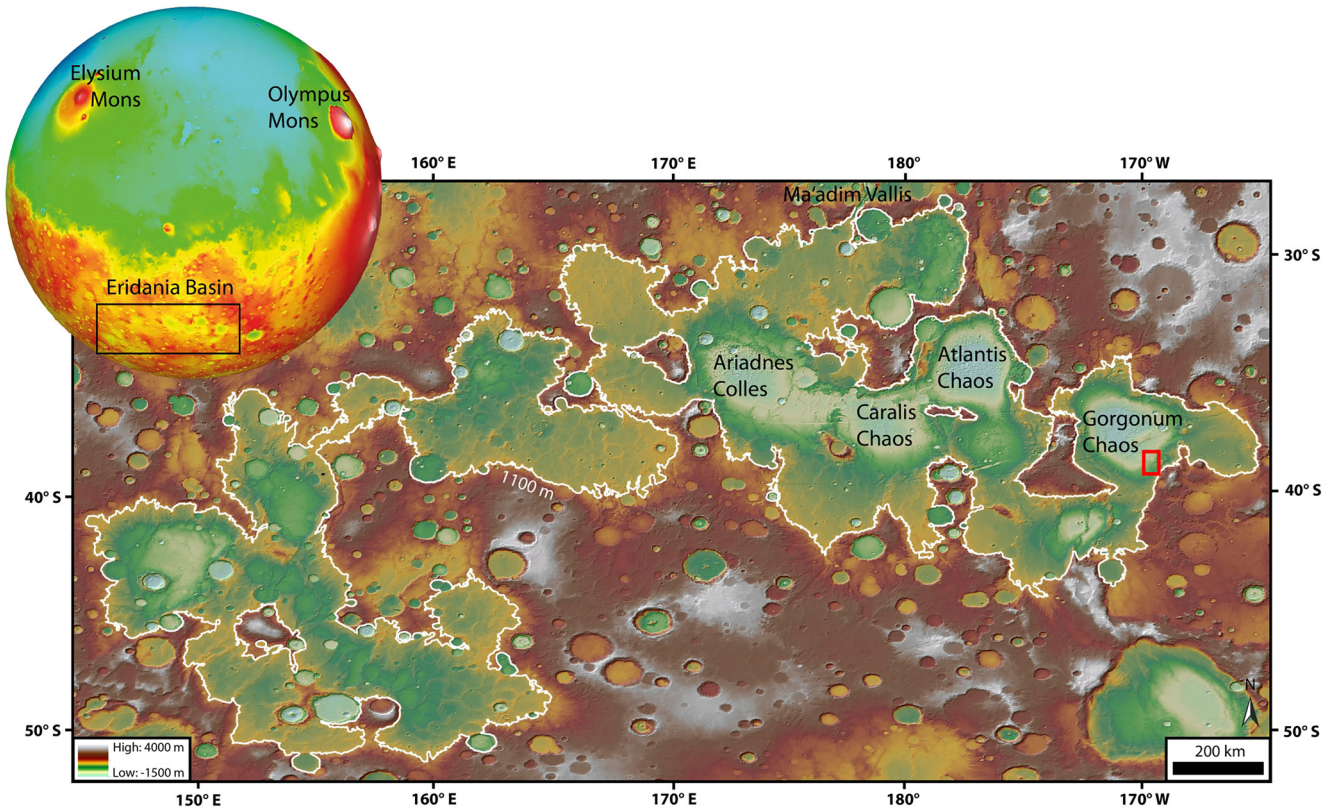

Figure 1. Cylindrical projected and color-coded Mars Orbiter Laser Altimeter (MOLA) digital terrain model (128 pixel/degree) of Eridania basin. The extension of the hypothesized paleolake is highlighted with the 1,100 m contour-line (Irwin et al., 2004) and the locations of the main sub-basins are marked with their names. The Ma'adim Vallis outflow channel is situated in the north of the basin. The extent of the study area is displayed as red frame in the southeast of Gorgonum Chaos.

best known for their ancient age, younger units can be found as well. Together, the diverse units in the highlands with their large age range offer the opportunity to study the aqueous evolution of Mars through time. The ideal places to do so are where units of a wide age range are exposed in close spatial neighborhood (e.g., at geological windows), where stratigraphical relationships are clearly visible. The aim of this work is a better understanding and the reconstruction of various aqueous phases and geochemical environments of Gorgonum Chaos through Martian history. The results shed light on the past climate change of the planet. We selected a study region at the southeastern rim of Gorgonum Chaos, the easternmost sub-basin of the Eridania basin and part of Terra Sirenum (Figure 1). The identification of Ma'adim Vallis as an outflow channel and supposed shore-lines at the 1,100 m elevation level (Irwin et al., 2002, 2004) led to the assumption that the Eridania basin hosted a paleolake near the Noachian/Hesperian boundary ~3.7 Ga (Irwin et al., 2002). At that time, the Eridania paleolake was probably drained through the Ma'adim Vallis channel (Irwin et al., 2004) and the region provides a record of the major geological events happening during and after its formation. Therefore, it is a prime site to study the past geological history of the Martian highlands.

1.2. Regional Setting

The eastern sub-basin Gorgonum Chaos has a diameter of ~240 km and a maximum depth of −400 m with respect to the supposed shorelines. From east to southwest, Gorgonum Chaos is cross-cut by the Sirenum Fossae, a graben system that extends radially from the Tharsis region (Wilson & Head, 2002). In the north and west of Gorgonum Chaos, the floor is dissected by numerous fluvial valleys and forms irregular knobs and mesas (Howard & Moore, 2011; Wendt et al., 2013). Craters larger than 20 km in the vicinity of Gorgonum Chaos are intensely eroded and mostly filled with sediments (Capitan & Van De Wiel, 2011). Howard and Moore (2004) report that the basin displays no large impact craters superposing the flat basin's floor and

that this basin was possibly covered by an ice-sheeted paleolake. Where the floor of the presumed paleolake crops out, it is characterized by light-toned material, which often consists of hydrated minerals or chlorides (Adeli et al., 2015; Glotch et al., 2010; Grant et al., 2010; Osterloo et al., 2010; Wendt et al., 2013).

The study area extends over 30 × 50 km and is centered at 38.75°S and 190.25°E (Figure 2). In the southeast the study area is limited by Gorgonum's rim and has a northwest slope of an average dip of 1.1° toward the basin center. The study area was selected because it offers prominent morphological and albedo features, which differ significantly from the rest of the basin floor. An infilled, heavily degraded crater with a diameter of ∼22 km occupies the east of the study area. Adjacent to this crater's western rim, a north-south elongated depression exhibits numerous morphologic features such as mounds, sinuous ridges and pits resulting in an irregularly shaped surface. At the surface of this depression, light-toned materials are exposed. In the western range of the study is a similar, but smaller depression. Here, the formation of different morphological features and the exposure of light-toned materials are limited to the vicinity of a small wrinkle ridge (Golombek et al., 2001; Schultz, 2000).

2. Data Sets and Methods

2.1. Imaging and Topographic Data

2.1.1. Images

Geological mapping and morphological investigations were based on images acquired by the Context Camera (CTX; Malin et al., 2007) and the High Resolution Imaging Science Experiment (HiRISE; McEwen et al., 2007) on board of the Mars Reconnaissance Orbiter (MRO) (see acknowledgments). CTX is a panchromatic camera that provides images with 30 km width and a scale of 6 m/pixel. The HiRISE camera produces 6 km wide images in the red spectral range (550–850 nm) with a nominal ground pixel size of ∼30 cm. HiRISE additionally provides color images of a 1.2 km wide area with measurements in the blue-green (400–600 nm) and infrared (800–1,000 nm) range.

2.1.2. Topography

The topography of surface features was analyzed via digital terrain models (DTM). A general topographic overview of the complete study area is provided by a DTM with a ground sampling distance of 125 m derived from stereo images acquired by the High Resolution Stereo Camera (HRSC; Gwinner et al., 2016) onboard the Mars Express Orbiter (MEX). In addition to the HRSC DTM, two high-resolution DTMs were generated from two stereo pairs of HiRISE images (ESP_048614_1410 and ESP_048825_1410; ESP_048469_1410 and ESP_047546_1410), using the open source software Ames Stereo Pipeline (ASP). Afterward, ASP was used to correlate the DTMs with topographic information from Mars Orbiter Laser Altimeter (MOLA; Smith et al., 2001). Based on the HiRISE images ESP_048825_1410 and ESP_048469_1410, the final HiRISE DTMs were orthorectified with ground sampling distances of 1 m. All datasets were merged into a GIS environment and projected into a sinusoidal projection to reduce geometric distortion.

2.2. Spectral Data

2.2.1. THEMIS

To investigate thermal infrared inertia, Thermal Emission Imaging System (THEMIS; Christensen et al., 2004) data on board the Mars Odyssey Orbiter were used. The multispectral sampling ranges from 5.5 to 14.9 μm in 10 channels and is provided with a spatial sampling of 100 m/pixel. Daytime and nighttime measurements cover the entire study area and were compared with each other to analyze thermal radiance of surface materials. This provides information about physical properties, such as induration, particle size, and density (Mellon et al., 2000; Pelkey et al., 2003; Presley & Christensen, 1997).

THEMIS data were also used to analyze the mineralogy. The decorrelation stretch (DCS) technique amplifies the contrast of uncorrelated multispectral bands and increases the potential to identify the composition of surface materials (Gillespie et al., 1986). Initial data are daytime measurements, using the sun as the light source. The result is a color-coded map of the observed area in which each color represents the predominance of a type of mineral. In this work bands 8 (11.8 μm), 7 (11.0 μm), and 5 (9.4 μm) of the THEMIS

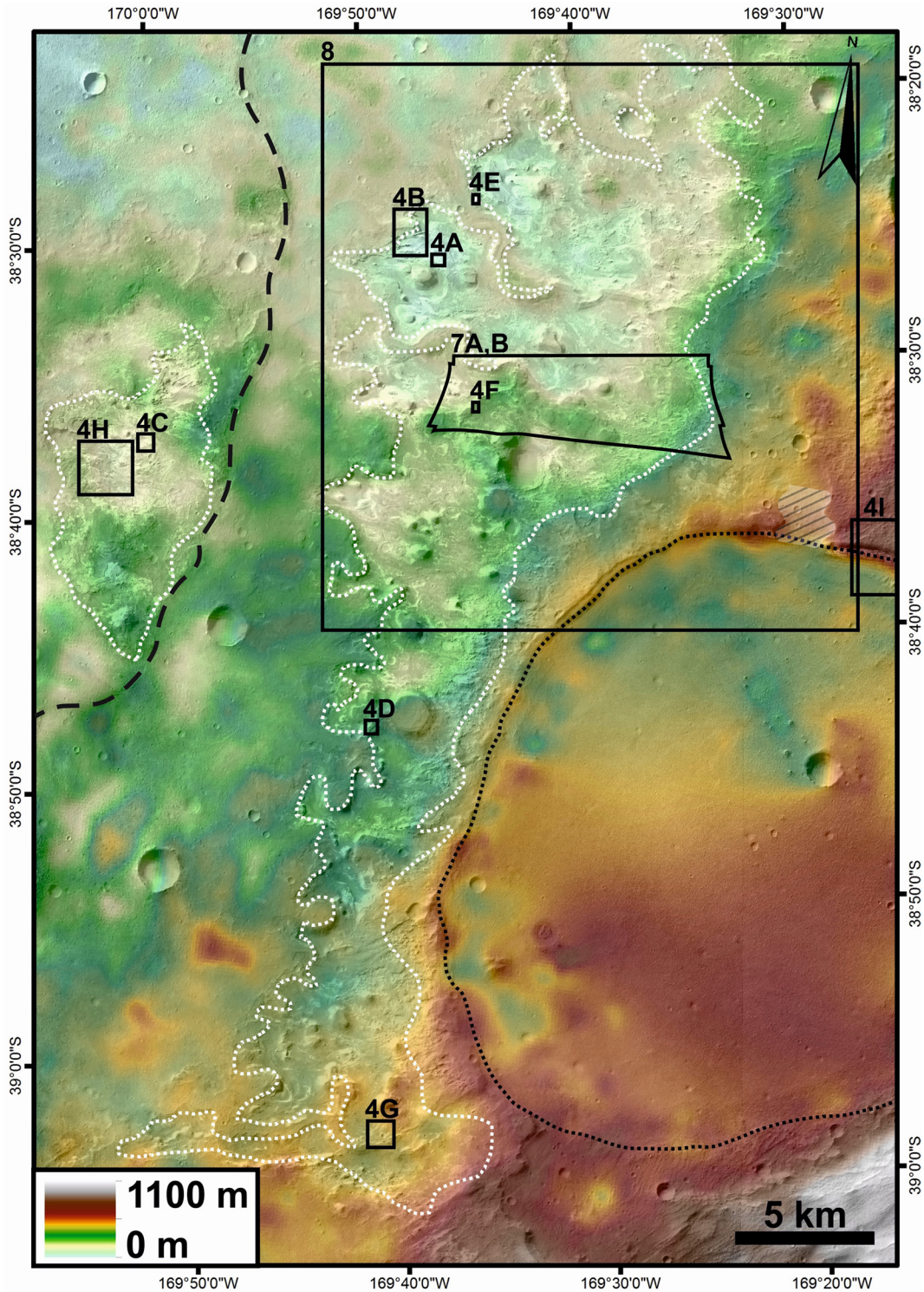

Figure 2. Overview of the study area based on Context Camera (CTX) imagery (6 m/pixel) combined with a High Resolution Stereo Camera (HRSC) derived digital terrain models (DTM) (125 m/pixel). In the southeast, the dotted black line marks a degraded crater with a prominent gap (dashed pattern). In the center and the west, the large and the small irregularly shaped depressions (dotted white lines) are encompassed by the flat basin floor. A wrinkle ridge in the northwest is highlighted with a dashed black line. Black boxes indicate the positions of enlarged figures in this study.

measurements are used in red, green, and blue (RGB). This is a standard combination, provided by the ASU THEMIS-database. Images processed with the 8-7-5 stretch were checked for their color consistency and different colors have been assigned to specific minerals (Glotch et al., 2010; Osterloo et al., 2010; Pan et al., 2015).

2.2.2. CRISM

Hyperspectral data are provided by the Compact Reconnaissance Imaging Spectrometer for Mars (CRISM; Murchie et al., 2007) onboard the MRO and were used to analyze the composition of surface material. The hyperspectral measurements cover a spectral range from 0.362 to 3.92 μm in 544 channels, each with a spectral resolution of 6.5 nm (Murchie et al., 2007). The total spectral range is divided into two datasets with the 1 μm wavelength as upper or lower limit, respectively. The short s-band represents visual (VIS) wavelengths and the longer l-band the near infrared (NIR) spectrum. We used CRISM data sets that cover the same area with minor offset and a spatial sampling of 13 × 16 m per pixel. Both data sets were collected in May 2016.

The resulting spectra are combined observations of the visual s-bands and near infrared l-band, both plotted into a single graph that terminates at 2.65 μm to cut off device-related disturbances. Using the CRISM provided CAT software in ENVI the results were corrected to minimize atmospheric (McGuire et al., 2009) and photometric (Murchie et al., 2007) influences. The obtained ratioed spectra were compared with the U.S. Geological Survey Digital Spectral Library (Clark et al., 2007) or spectra published in the PDS Geosciences Spectral Library by Bishop et al. (2008).

2.3. Age Determination

The absolute model age determination was obtained by analyzing the crater size-frequency distribution. As counting areas, flat terrains with minor resurfacing effects and degradation were chosen. Craters with a diameter larger than 50 m were mapped at a scale of 1:15,000 with the CraterTool extension (Kneissl et al., 2011) in an ESRI ArcGIS 10 environment. We used the Craterstats2 software (Michael & Neukum, 2010) to model the crater size-frequency distribution, applying the chronology function of Hartmann and Neukum (2001) and the production function of Ivanov (2001). The randomness of crater populations was tested with the method of Michael et al. (2012) to avoid secondary craters.

To constrain the age of the complex landforms, based on CTX images, 470 craters have been counted in the northwest of the study area on an area of 360 km^2. A second crater count was obtained in the southeast of the study area with an extent of 315 km^2 that gives the maximum model age of the surface.

3. Results

3.1. Morphology

3.1.1. Southeastern Crater

From the southeastern rim of Gorgonum Chaos the terrain descends steeply from 1,100 m to 500 m altitude where the filling of the adjacent 22 km diameter impact crater forms an approximately horizontal plain (Figure 2). The altitude of the crater filling plain changes insignificantly from east to west and from south to the crater's center. To the crater's northern rim the plain gently slopes to 300 m. The crater is bounded by degraded walls whose crests descend outwards to the surroundings at an elevation of 100 m. The northern crater wall is breached by a prominent gap near the area where the crater plain reaches its topographically lowest altitude. The 1,500-m-wide and 60-m-deep gap continues as a broad sinuous valley toward the north.

3.1.2. Depressions

In the study area, two depressions have evolved in the basin floor. To the west of the southeastern crater a large depression extends over ∼380 km^2 that displays distinct signs of degradation (Figure 2). The floor of the 45 × 12 km, north-south oriented large depression slopes from east to west. In the east, the transition from the basin floor into the depression is gradational and defined by gentle slopes or minor terraces. The western rim of the large depression is characterized by two terraces. The altitude difference between the

floor of the depression and the basin floor is up to 150 m. The two terrace floors consist of significantly polygonized horizons of light-toned material.

The second depression covers an area of ~50 km^2 with an extent of 11 × 6 km. A wrinkle ridge, up to 500 m wide, crosses the study area from north to west and forms the eastern limit of this less extended depression. The highest elevations in this smaller depression are crests of the wrinkle ridge, which rise up to 70 m above the surrounding basin floor. The flanks of the crests steeply slope toward the depression floor, whose lowest point lies ~100 m below the non-eroded basin floor.

3.1.3. Sinuous Ridges and Circular Mounds

The two depressions are characterized by a number of positive topographical features. Several sinuous ridges cross the large depression from east to west. The top surfaces of these sinuous ridges are flat and at the same elevation as the surrounding basin floor. Occasionally, a narrow trough marks the center of the ridge and follows its bends. The flanks slope down at an average angle of 25° and layering is often traceable over several hundreds of meters. The lateral width of the ridges substantially widens downslope from east to west. Only a few ridges cross the depression over its whole width and are traceable over a length of more than 15 km.

Another class of topographical features at the depression floors are circular mounds with diameters ranging from 0.5 to 2 km. Their top levels are at the same elevation as the surrounding basin floor and are covered with a 2–3 m thick layer of dark material. The mounds have flank slopes between 15° and 25° and rise up to ~200 m above the ground of the depression. The western rims of some circular mounds with diameters larger than 1 km are the starting point of some sinuous ridges. At the point of contact between sinuous ridge and circular mound, both features have the same elevation that is comparable to the estimated uneroded basin floor.

In addition to circular mounds, several buttes with an irregularly shaped plan view range in their base diameters from 0.3 to 1 km. Large buttes frequently have an elongated shape with a west-northwest to east-southeast orientation. The top levels of buttes typically rise 50–100 m above the surface of the depression, but are less elevated compared to the top level of sinuous ridges and circular mounds. A distinctly polygonized layer on the top of buttes is related to the altitude of the terraces at the rim of the depression. This layer terminates in rough and nearly vertical scarps.

3.1.4. Pits

Several isolated pits are present on the bottom of both depressions. Based on measurements on HiRISE-derived DTMs the pits are ~20 m deep, have an elliptical plan map shape, and a bowl-shaped cross-sectional profile. Their long axes range between 200 and 800 m in length and are oriented in a west-northwest to east-southeast direction. In the west of the large depression, the pits increase in size and merge to extended systems of incisions with a depth up to 50 m. Numerous parallel transverse aeolian ridges (TARs) (Balme et al., 2008) appear at the bottom of the pits. These TARs have a general north-northeast to south-southwest orientation and an either solidified or unconsolidated appearance. Their observed heights exceed 3 m and reach lateral lengths of several hundreds of meters.

3.2. Geological Unit Description

Based on the imagery data of HiRISE and CTX, we created a geological map of the study area that displays five geological units (Figure 3). In addition, the wrinkle ridge and major channel systems are documented. The mapped geological units are distinguished by their texture, brightness, and color. These geological units are a light-toned polygonized unit (lNlp) at the floor of the depressions, an only locally appearing ridge unit (NHr), a light-toned rugged unit (NHlr) that is also found in the depressions, and a widespread dark cap unit (Adc) that covers the majority of the basin floor and minor areas of the depressions. A thin and smooth unit (lAs) covers the surface in the east of the map.

3.2.1. Late Noachian: Light-Toned Polygonized Unit (lNlp)

A unit of light-toned material is exposed at the floor and flanks of the two depressions. It has a smooth surface and is gently undulating. Its appearance is irregularly polygonized with an average polygon diameter of

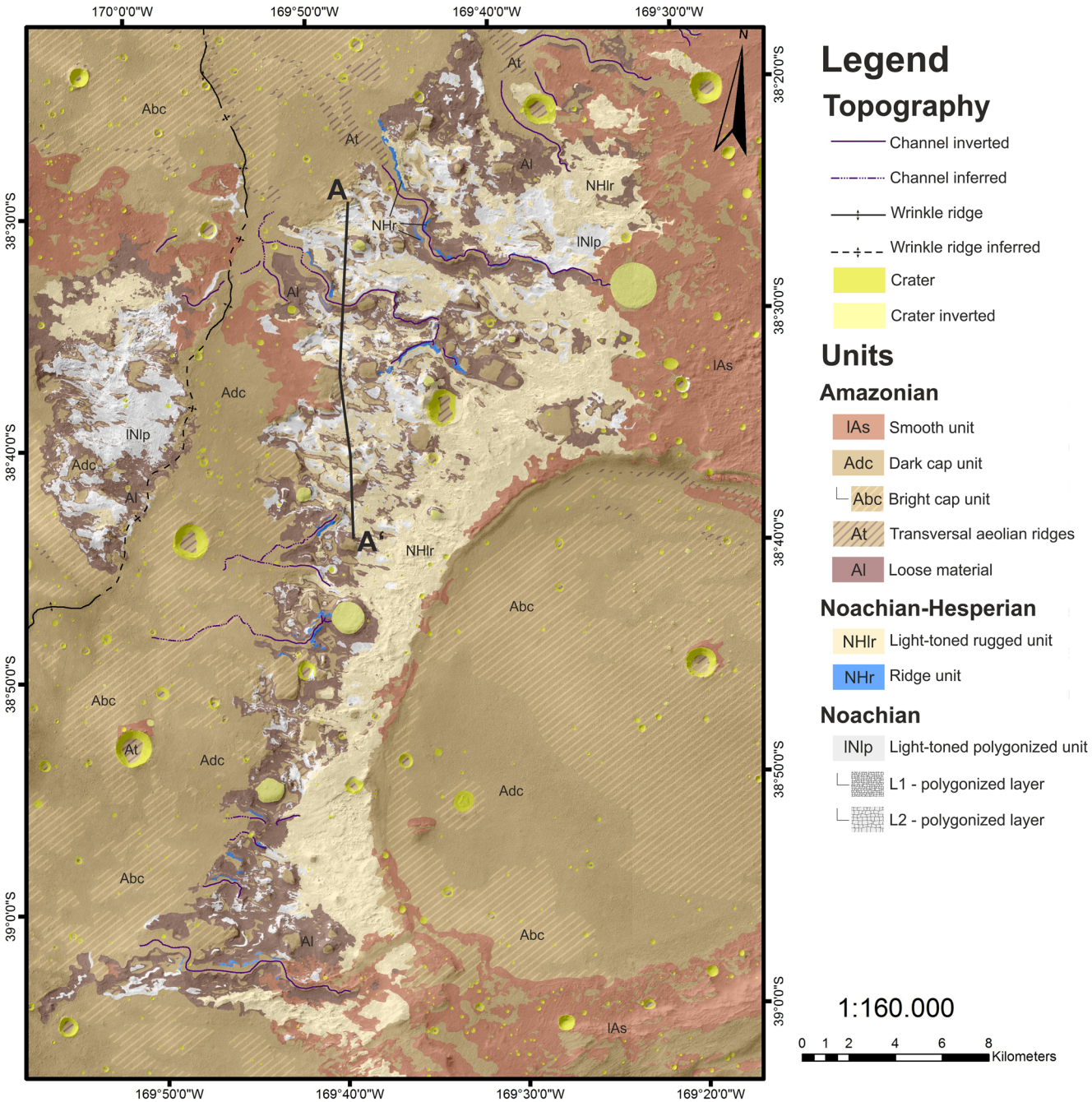

Figure 3. A geological map of the study area overlain on Context Camera (CTX) images. Geological units as well as major topographic features are displayed in this map.

less than 5 m (Figure 4a). This unit presents two distinct layers L1 and L2 that are characterized by polygons larger than 5 m and in the formation of two terraces (Figure 4b). The lower L1 layer crops out where erosion has cut a series of pits into the floor of the larger depression. These pits exclusively occur within unit lNlp and layer L1 represents their upper rim. Several pits display curvilinear albedo-features that result from deposited dark sand or ash and trace the layer (Figure 4c). Within layer, L1 polygons are slightly larger than ~5 m, but are more emphasized compared to the surrounding material. This layer is traceable over several kilometers, presenting a constant thickness of ~15 m. The second, upper layer L2 abundantly appears as the top layer of buttes. The individual polygons in this layer appear less firmly connected to each other

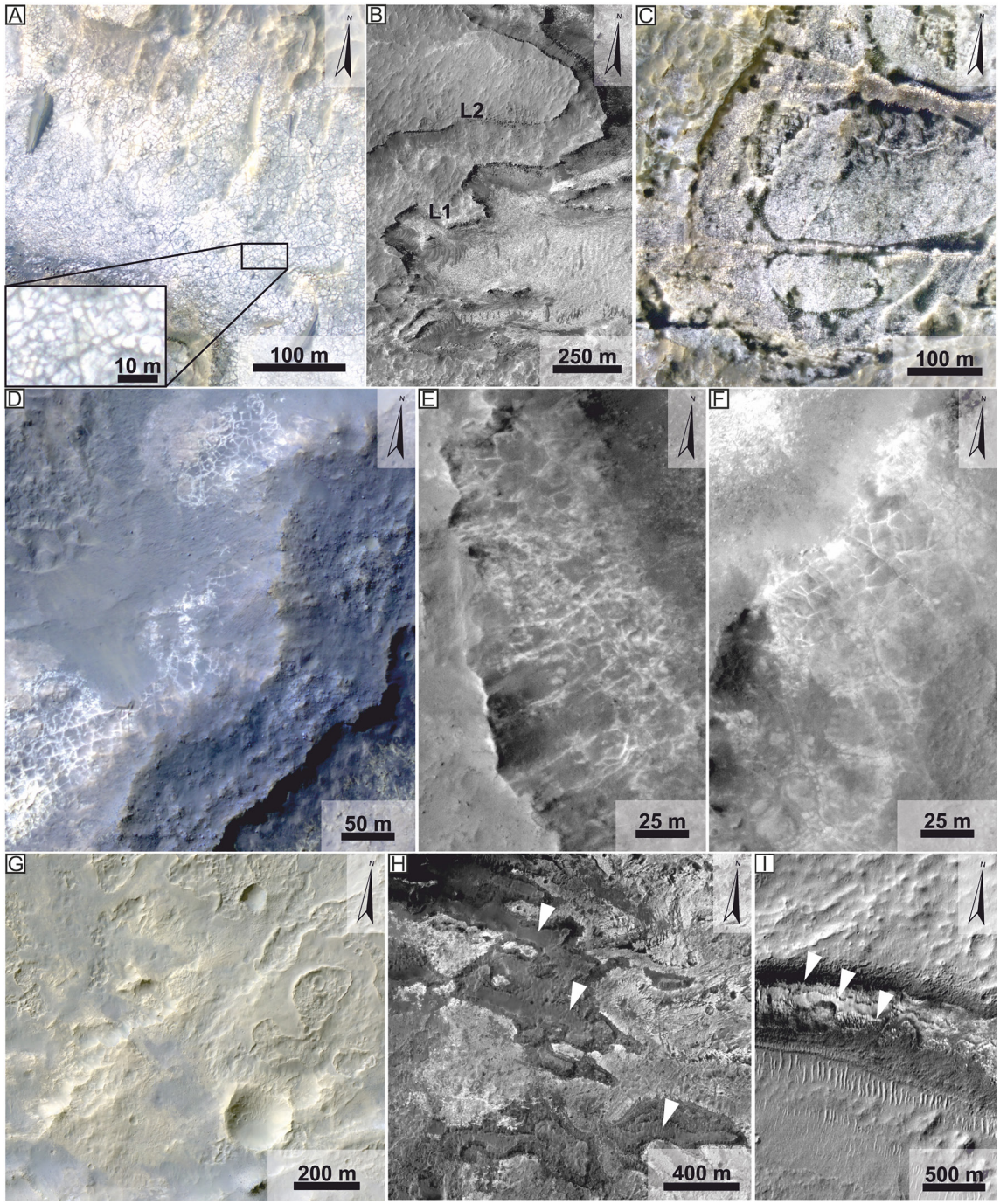

Figure 4. Morphologic details of five geological units, shown at HiRSE images (0.3 m/pixel). Colored images are in IRB combination. (a) Light-toned and distinctly polygonized unit lNlp. The inset shows an enlarged view of the polygons. (b) Terraces at the western rim of the large depression. The topographically lowest level in the southeast (lower right) is the bottom of the depression, the middle level represents layer L1 within lNlp, and the upper level reflects layer L2. (c) Curvilinear structures in some pits suggest a layering of unit lNlp. The dark material is accumulated sand or dust. (d–f) Unit NHr crops out at upper flanks of sinuous ridges and is characterized by irregular polygonization and bright material in refilled cracks. (g) Shown is the surface of unit NHlr. (h) A thin layer of Adc forms elongated structures (white arrows) and overlies lNlp. (i) Bright unit lAs at the south-facing slope of the southeastern crater rim. The white arrows point to distinctly visible layers of the unit. In the lower half of the image north-south oriented TARs are visible. Image references: panels (a, b, e, f): HiRISE ESP_047546_1410; panels (c, h): HiRISE ESP_048614_1410; panels (d, g): HiRISE ESP_045977_1405; panel (i): CTX J03_045766_1410.

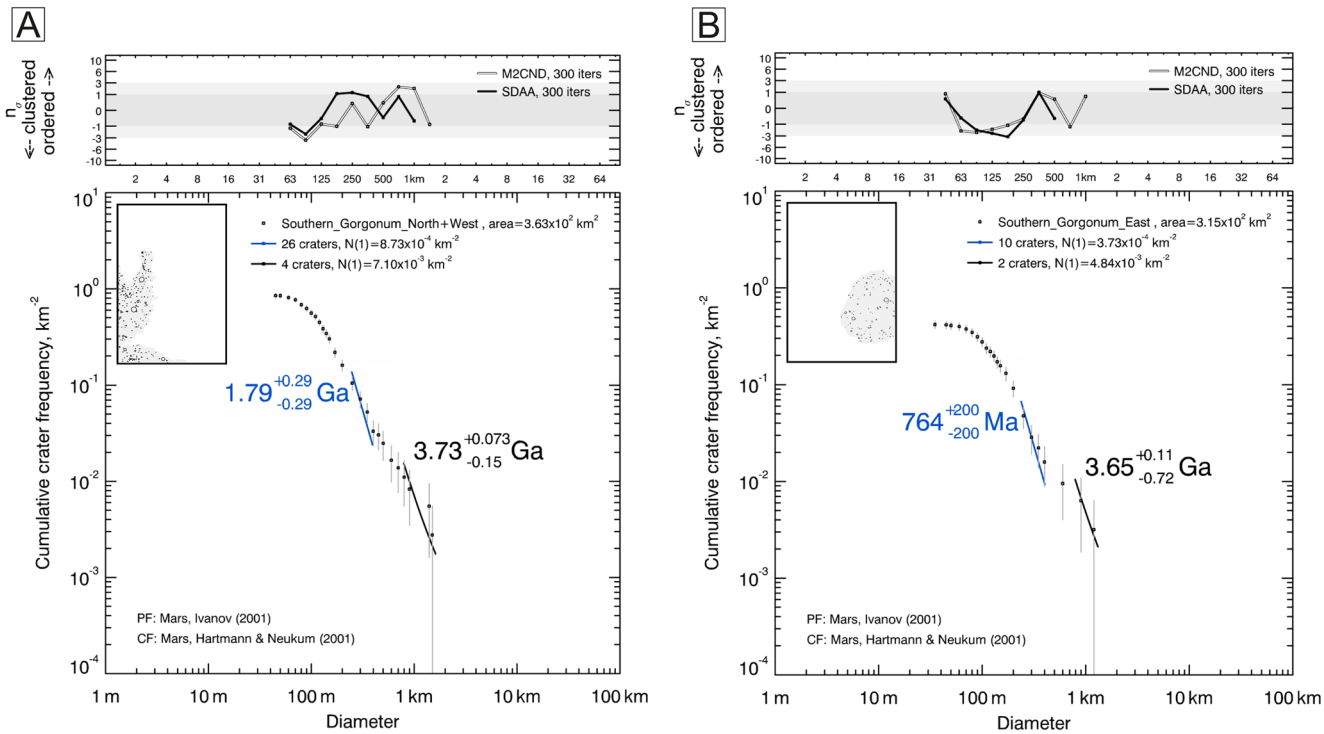

Figure 5. Absolute model ages of (a) the flat basin floor and (b) the southeastern crater filling. The model age of lNlp is displayed in black and of draping unit Adc in blue. The upper left boxes represent the extent of the study area and the gray shadow the position of the crater counting area. The plots on top display the randomness of the crater distribution in the counting area. Values between −1 and 1 mean ideal randomness, the gray zone is still acceptable.

and at steep slopes appear to be separated blocks. The L2 layer is ~30 m thick and is traceable over tens of kilometers. Comparisons with other regions of Gorgonum Chaos make it very likely that lNlp forms most of the Gorgonums basin floor.

The absolute model age of the unit was calculated from two crater counting areas. The first crater counting area was the non-eroded basin floor in the southwest of the study area and gives a minimum model age of late Noachian 3.73 Ga (+0.07/−0.15 Ga) (Figure 5a). Although the surface is covered with an Amazonian dark cap unit (Adc), this unit is thin enough that larger craters in the underlying unit lNlp can be detected. The plain floor of the southeastern crater was the second counting area. The result is based on comparatively few craters and gives an estimated model age of about 3.65 Ga (+0.11/−0.75 Ga) (Figure 5b). This age is slightly younger, but still within the error tolerance of the age determination of the southwestern basin floor. Both modeled ages indicate a unit formation during Late Noachian (Michael et al., 2012).

3.2.2. Noachian-Hesperian: Ridge Unit (NHr)

The upper surface of sinuous ridges and circular mounds consists of a unit with irregular polygonization (Figures 4d–4f) and a distinctly lower albedo than lNlp. This unit has a thickness of ~20–25 m and the size of the polygons is about 10 m in diameter. The polygons are separated from each other by high-standing material that is significantly brighter than the polygons and appears like refilled cracks. At some ridges, the unit shows subtle layering which is traceable over several hundreds of meters. Due to the limited observable surface area, an absolute age determination of the unit via crater counting is not feasible. Its maximum age is limited by the underlying Late Noachian lNlp and the minimum age may reach far into the Hesperian before the next younger unit was deposited.

3.2.3. Noachian-Hesperian: Light Rugged Unit (NHlr)

A bright unit without signs of polygonization is exposed within the larger depression adjacent to its eastern rim. Its albedo appears slightly lower than of unit lNlp, which is directly beneath. The thickness of unit NHlr varies significantly; at the bottom of the depression, the unit covers the underlying lNlp only 2–6 m

thick and often allows the observation of the underlying unit. Within the depression, the surface of the unit is highly irregular and gives a rugged and unstructured appearance. To the east and south, the surface becomes more planar (Figure 4g) and the thickness of the unit increases to an indefinable level, since no lower boundary is observable.

Due to the irregular and rugged surface of the unit, the number and size of existing craters cannot be determined and an absolute age modeling is not feasible. NHlr was deposited on top of lNlp and NHr. For that reason, the maximum age is younger than the age of ridge-forming NHr. The minimum age is not possible to determine and may extend far into the Hesperian.

3.2.4. Amazonian: Dark Cap Unit (Adc)

The noneroded basin floor of southeastern Gorgonum Chaos is flat and covered by layer Adc that appears sandy or dusty at its surface. Single boulders of ∼1–2 m size accumulate where this unit terminates. The albedo of this capping unit is considerably lower than that of the underlying units in the study area (Figure 4h). In high-resolution images, the dark cap appears locally solidified and does not exceed a constant thickness of ∼2–3 m. In addition to the flat basin floor, this unit is also deposited on top of sinuous ridges, circular mounds, and buttes. The crater counting at the southwestern flat basin floor suggests an age of ∼1.79 Ga (±0.29 Ga) (Figure 5a). A second crater counting at the surface of the refilled southeastern crater reveals a surface age of ∼764 Ma (±200 Ma) (Figure 5b). Despite their discrepancy, both modeled ages indicate a formation age of this unit during the Amazonian period.

In both depressions, this dark cap occurs with limited lateral extent, linked to local topography. The unit forms single patches or elongated structures with a width of about 150 m and a length up to 3 km, oriented in a west-northwest to east-southeast direction (Figure 4h). This is the same orientation of elongated pits, buttes, and TARs.

Adc seems to form a different subunit in different places. On top of the noneroded basin floor, HiRISE images reveal areas of Adc of considerably higher brightness and of variable extent. These areas of Adc are characterized by a subunit of unconsolidated Amazonian bright material (Abc), which forms small-scaled ripple-structures on top of distinctive flat areas.

3.2.5. Amazonian: Transversal Aeolian Ridges (At) and Loose Material (Al)

At is characterized by areas with TARs and has been developed on top of Adc, on the bottom of the depressions, and large craters. The albedo of the TAR material varies considerably between different places. In the depressions, the albedo of some adjacent TARs differs significantly between that of unit Adc and extremely dark areas. The dominating orientation of the crests of the TARs is from south-southwest to north-northeast (Figure 4i). Our DTM-based measurements show that the crests exceed an elevation of 3 m above the surrounding terrain and a lateral extent of several hundreds of meters. A distinct age determination of the TARs is not possible, but occasionally underlying Amazonian units and their undegraded surface suggest an Amazonian age.

At the inner rims of both depressions and at the base of sloped features, a unit of loose material was deposited. This Amazonian loose unit (Al) covers local areas of the depressions floor and appears much thinner than Adc. It has a uniform and smooth surface, is of similar albedo as unit Adc and is probably material that was transported away from unit Adc and was deposited elsewhere.

3.2.6. Late Amazonian: Smooth Unit (lAs)

CTX images show that the northeastern study area and the heights adjacent to the southeastern crater are covered by a few meters-thick and smooth unit. The unit extends with constant thickness atop plains, rough terrains, or at crater walls and comprises no visible structures. Numerous irregular shaped windows were formed and reveal an uneven underlying surface. At south-facing slopes of the southeastern crater rim the unit appears much thicker and presents distinct few meters-scaled layering (Figure 4i). Where dust does not cover the unit, it appears very bright compared to the surrounding material. In CTX images, the unit lacks visible fresh, superposed impact craters, indicating a very young Late Amazonian age. Erosion of potential craters leading to a preimpact unit appearance is unlikely. Since the unit is very thin, the complete erosion of craters would also erode the unit itself.

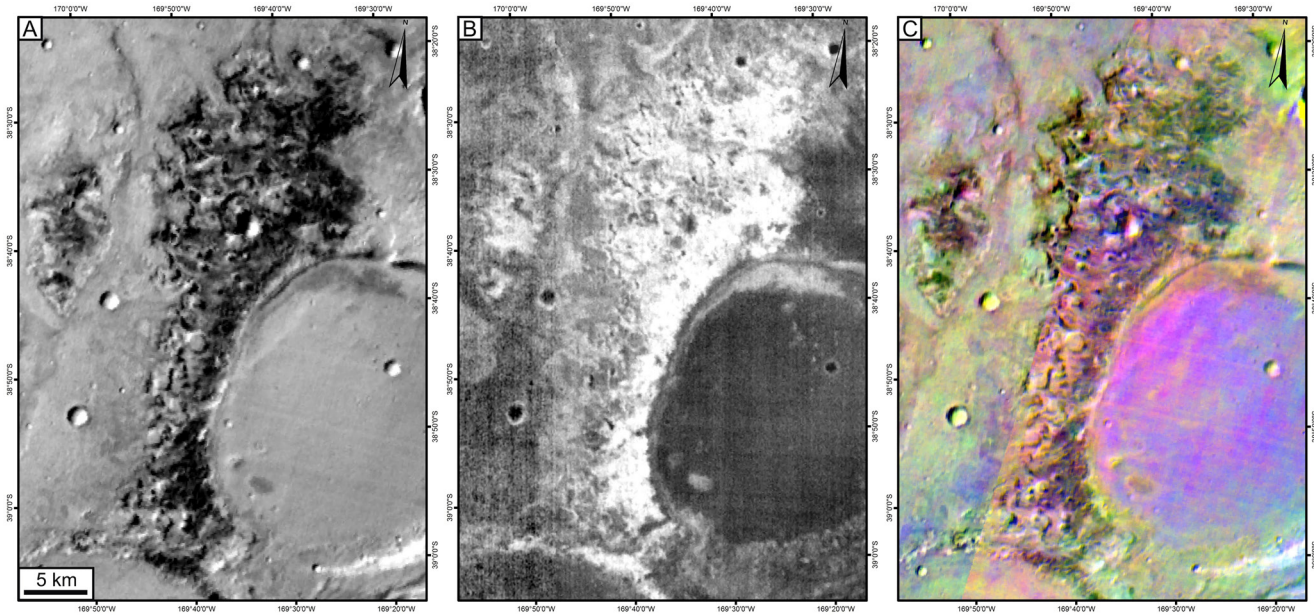

Figure 6. Thermal Emission Imaging System (THEMIS) imaging of the study area. (a) In thermal infrared (TIR) radiance during daytime, the depressions appear very dark. (b) The TIR radiance of the same area during nighttime. Here the depressions appear very bright. (c) A false-color image of the daytime TIR radiance in decorrelation stretch (DCS) 8-7-5 bands in RGB combination. Olivine appears purple and pyroxene green (Pan et al., 2015). The figure is a combination of two images with a visible boundary.

3.3. Thermal Analysis and Spectroscopy

3.3.1. Thermal Analysis

3.3.1.1. Daytime IR

Daytime THEMIS data display high variations in their infrared brightness (Figure 6a). The overall variation of daytime surface temperature in the region is 29 K. Two distinct regions with low infrared brightness correlate very well to those regions that are geological mapped as lNlp and NHlr (Figure 3) and indicate the lowest surface-temperatures in the study area. They stand out against the surrounding flat basin floor and demonstrate the complex morphology of the depressions at a hundred meter scale. The flat basin floor surrounds the low infrared brightness areas by presenting an increased and slightly varying infrared brightness.

The spectra of brightest and warmest regions are dominated by slope effects. Northwest-facing crater walls are sun-exposed and thus distinctly warmer than southeast sloping walls. Therefore, the thermal signature of steep slopes does not contribute useful data to a material analysis.

3.3.1.2. Nighttime IR

Two THEMIS nighttime datasets were used to analyze the study area. I02684006 was acquired during southern Martian autumn and delivers surface temperature variations of 24 K. I07902021 displays surface temperature variations of 14 K during southern Martian summer. Despite the seasonal and temperature offset between the two datasets, they provide comparable results: The temperature differences are reversed to the contrary compared to daytime measurements that low infrared brightness regions display the highest brightness during nighttime (Figure 6b). The basin floor displays moderate to low thermal signatures relative to the regions of high infrared brightness. The surface of the southeastern crater filling appears considerably darker and more uniform than the basin floor in the western parts of the study area. The boundaries between units of high and low infrared brightness are sharp and enable a clear distinction of morphological features.

These observations indicate that the depressions are characterized by materials with increased thermal inertia, which store thermal energy more effectively and suggests solid rock exposed at the surface (Fergason et al., 2006), in contrast to the flat basin floor that is covered with less competent to unconsolidated Adc.

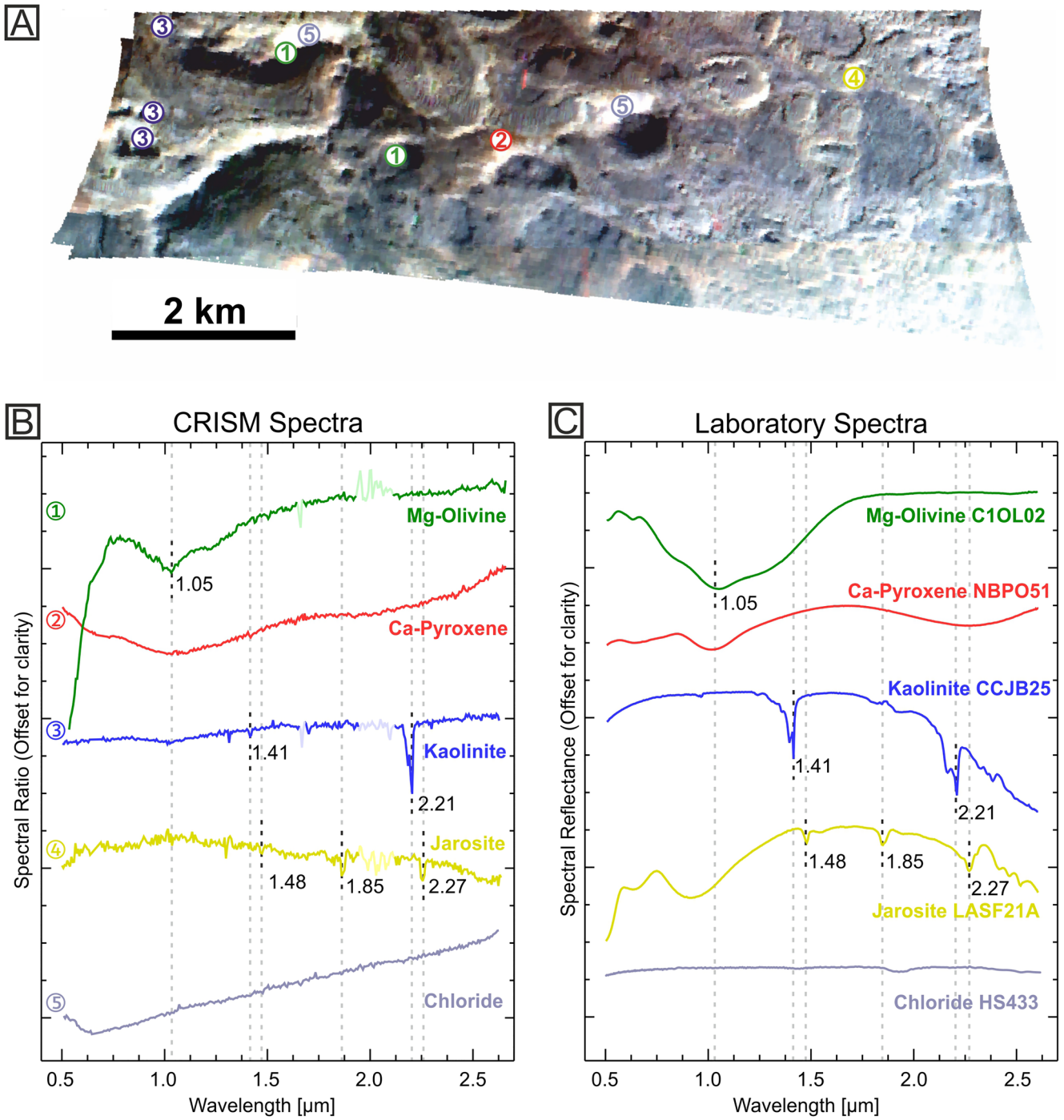

Figure 7. Spectra of the surface obtained from Compact Reconnaissance Imaging Spectrometer for Mars (CRISM) data. The geographic position of the datasets presented in panels (a) and (b) are marked in Figure 2. (a) Locations of analyzed spectra are marked with colored numbers on a false-color image (red: 2.5 µm; green: 1.5 µm; blue: 1.08 µm). (b) Ratioed CRISM spectra that are related to the marked positions in (a). Noise signals at 1.65 µm and around 2 µm are partially masked. (c) Shown are laboratory spectra (Clark et al., 2007) of analog materials to compare with CRISM spectra.

3.3.2. Spectroscopy

Most of the study area is covered by dust and therefore spectra are not suitable for the determination of minerals beneath. In this study, most analyzed CRISM spectra were obtained at dust-free and north-facing slopes, where insolation by the sun is higher (Figure 7a).

The spectral ratio BD1900R (Viviano-Beck et al., 2014) was used to get a general overview of the occurrence of hydrated minerals. With this ratio a strong absorption band at 1.9 μm was observed exclusively at unit lNlp and NHr. This narrow absorption band at 1.9 μm is related to H-O-H stretching and indicates the presence of hydrated minerals such as phyllosilicates, sulfates, and hydroxides (Clark et al., 1990). NHlr and Adc display sparse to no such signals. A detailed classification of hydrated minerals such as phyllosilicates or sulfates is not possible with the ratio BD1900R and was done by a more precise analysis of local spectra. A further significant absorption band at 1.4 μm, caused by the O-H stretch (Clark et al., 1990), is an additional indicator of hydrated minerals. Due to weak signals of this band in our data, the spectral ratio does not enable any robust detections.

3.3.2.1. Al-Phyllosilicates

Unit lNlp crops out at several locations in the western parts of the two CRISM data sets. The measurements reveal a very prominent absorption band at 2.21 μm and a less expressed band at 2.19 μm (Figure 7b). This doublet is indicative for Al-OH vibrations (Clark et al., 1990). A spectral artifact can be excluded due to similar signals at different locations where this unit crops out. A much less pronounced, but recognizable absorption band at 1.41 μm indicates hydroxyl groups (Clark et al., 1990). This band is significantly reduced as compared to those of laboratory spectra, though observable at the predicted wavelength. Therefore, the spectra are interpreted as related to Al-phyllosilicates and likely to kaolinite, with laboratory spectra comparable to CCJB25 (Bishop et al., 2008) taken as reference (Figure 7c). The discrepancy between expected and observed signal strengths might be explained by imprecise atmospheric corrections or a decreasing performance of the CRISM instrument itself.

3.3.2.2. Sulfates

In the east of the CRISM data sets, corresponding to an outcrop of layer L1 in unit lNlp, absorption lines at 2.27 and 1.85 μm are detected. Absorption bands around 2.4 μm frequently result from hydrated sulfates and their combinations with water (Cloutis et al., 2006). Absorption bands around 1.9 μm might be related to stretching and bending vibrations of polyhydrated sulfates (Cloutis et al., 2006). A third band, characteristic for sulfates, is may be located at 1.48 μm, but difficult to recognize due to the background noise. Comparison with analog laboratory spectra of LASF21A (Bishop et al., 1995) might suggest the presence of jarosite (Figures 7b and 7c). However, due to the background noise, this is not certain.

3.3.2.3. Chlorides

Where NHr crops out, CRISM spectra lack distinct absorption bands, but are characterized by constantly increasing reflectance to higher wavelengths until 2.65 μm. This otherwise featureless appearance of spectral data is unique to chlorides (Glotch et al., 2010; Viviano-Beck et al., 2014). As a reference to verify supposed chlorides, we used laboratory measurement HS433 from the USGS Digital spectral library (Clark et al., 2007) and data provided by Viviano-Beck et al. (2014).

Chloride-bearing materials have also been observed in THEMIS DCS 8-7-5 data, where minor blue-colored areas are related to chloride-rich material (Osterloo et al., 2008, 2010). At these locations NHr crops out at sinuous ridges and circular mounds within the large depression. These spectral features corresponds to CRISM data, but an exact correlation of the THEMIS data to a distinct unit is difficult, due to their low spatial resolution.

3.3.2.4. Olivine

CRISM data from several Adc outcrops show a broad and deep absorption band centered at 1 μm and a shoulder around 1.2 μm. From 1.5 μm to higher wavelengths the spectra show no prominent absorption bands. According to Burns (1993) and the C1OL02 laboratory spectrum from the PDS Geosciences Spectral Library, the analyzed spectra match well with those of magnesium-rich olivine.

The distribution of Adc matches with an increased purple coloring at THEMIS DSC 8-7-5 data (Figure 6c) that is also indicative for a surface dominated by olivine (Pan et al., 2015). Notably, the surface of the southeastern crater is characterized by an almost homogeneous purple coloring in THEMIS DSC data. Additional purple signatures are less intense in the northern and western parts of the study area and within the depressions (Figure 6c).

3.3.2.5. Pyroxene

Some CRISM spectra of Adc display two very broad absorption bands from 0.8 to 1.4 μm and from 1.8 to 2.5 μm. Due to the stretching of the detected bands, a clear identification is difficult. Broad bands around 1 and 2.3 μm suggest calcium-rich pyroxenes (Burns, 1993). An additional signal of low absorption at 0.8 μm makes a correlation to sample NBPO51 (PDS database) reasonable and supports the identification of calcium-rich pyroxene. In THEMIS DSC 8-7-5 data, Adc also equals to a green color coding in addition to purple (Figure 6c) and is also related to pyroxene-rich surface material (Pan et al., 2015). This is because Adc was defined in an imagery mapping and not in a spectral mapping.

Sand or dust enriched with iron oxides cannot be ruled out as alternative source of the detected spectra, due to strong absorption bands of iron oxides around similar wavelengths.

3.4. Stratigraphy

The late Noachian light-toned polygonized unit (lNlp) is the oldest observable material in the study area. Where depressions have been eroded into the basin floor, this unit presents a thickness of at least 200 m (Figure 8a). The lower limit of lNlp and therefore actual thickness is not observable. The unit includes two layers with varying grade of polygonization. The lower layer L1 forms significant amounts of the ground level of the large depression and is about 15 m thick (Figure 8a). The upper layer L2 commonly forms the top layer of buttes and is approximately 30 m thick. The vertical distance between the two layers varies from more than 100 m in the center of the study area to 20 m in the north toward the center of Gorgonum Chaos.

Unit lNlp is directly overlain by Noachian/Hesperian ridge units (NHr) (Figure 8b) that forms the unit of sinuous ridges and circular mounds. It is the stratigraphically oldest unit after the basin floor (lNlp). NHr appears at isolated locations of limited lateral extent and is ∼25-m thick. The elevation of its upper level is approximately equal to that of the inferred basin floor.

In depressions and to the east of the study area, lNlp is overlain by the Noachian/Hesperian light rugged unit (NHlr). Within the large depression NHlr often lies directly on top of layer L1, but it can also be locally less elevated than surrounding features composed of older lNlp. This indicates that NHlr has been deposited after the formation of the depression and the disconformity between lNlp and NHlr marks a stratigraphic hiatus between both units (Figure 8b).

At the basin floor and within the depressions all units and the preexisting morphology are draped by Amazonian dark cap unit (Adc) with constant thickness. All previously described units are occasionally covered by TARs (At) of Amazonian age. The lateral extent of contiguous areas with TARs varies from several kilometers at the flat basin floor to isolated features at the bottom of pits in unit lNlp or atop NHr.

Predominantly in the east and south of the study area, the Late Amazonian smooth unit (lAs) seems to superpose the rugged surface of NHlr and Adc. In CTX images, lAs appears as the uppermost and therefore youngest mapped unit in the study area.

4. Discussion

4.1. Liquid Water

4.1.1. Formation of Basin Floor Until Lake Drainage

The bowl-shaped morphology of Gorgonum Chaos (Wendt et al., 2013) with its generally flat surface indicates a uniform deposition of unit lNlp, which conforms with the slope of the basin floor. The source material of lNlp could have been dust, volcanic ashes, or fine sands, transported via air fall to the surface of the hypothesized paleolake and subsequently sunken down to the bottom of the paleolake. The formation of lNlp from fluvially transported debris from higher elevations around the basin is less likely, since no alluvial fans, river deltas or other signs of transported clastic material were observed. This alternative transport process would result in less uniform and more uneven morphology of the floor near the rim of Gorgonum basin.

Within the unit lNlp, we observed outcrops rich in phyllosilicates (Figure 7). There are several potential formation processes for these phyllosilicates. Either the phyllosilicates were formed in situ by chemical

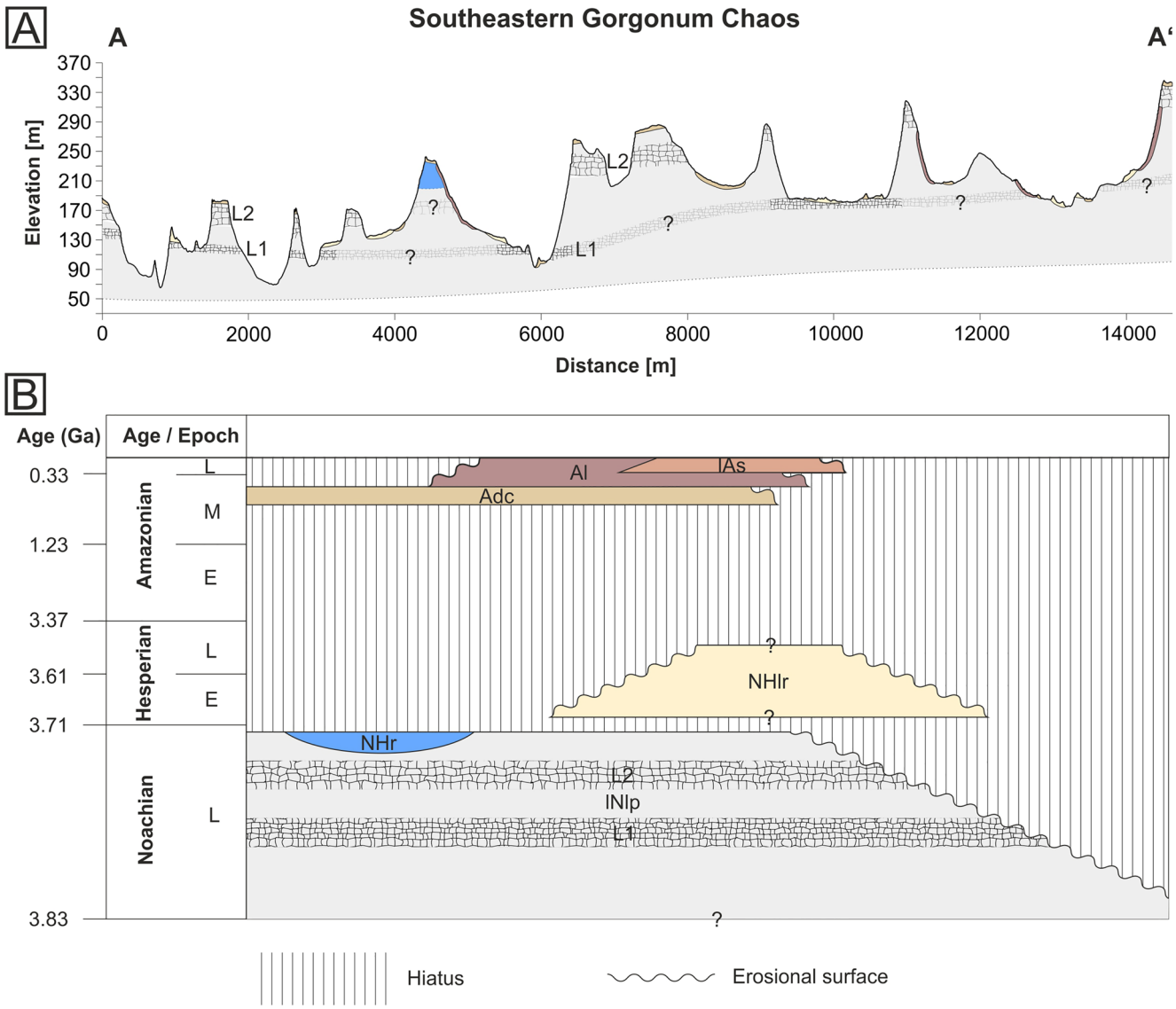

Figure 8. (a) The interpretive cross section of profile line AA′ (drawn in Figure 3) is based on a High Resolution Imaging Science Experiment (HiRISE) derived digital terrain models (DTM). The terrain is exaggerated by factor 10 and the color of the units relates to those of the legend of the geological map (Figure 3). (b) A chronostratigraphic column displaying the mapped units in their relations with each other.

alteration after the postulated air fall material came in contact with the water of the paleolake. Alternatively, the air fall material could already have contained the phyllosilicates or a rising water table altered the material after its deposition (Grotzinger et al., 2005). A combination of these processes seems also plausible. Which of the mechanisms was the dominant, one cannot be determined with the available data. In all cases, the accumulation of kaolinite in lNlp indicates that the material had to go through a process that enriched Al-phyllosilicates.

The upper layers of unit lNlp lack possible Fe/Mg-phyllosilicates that could have been transported away. As reported elsewhere on Mars (Carter et al., 2015; Le Deit et al., 2012; Loizeau et al., 2018), during periods of relative humidity, water could have transported away mobile Fe/Mg-ions from upper layers of the unit, resulting in an enrichment of Al-phyllosilicates, (e.g., kaolinite) at these locations. The upper layers in which Fe/Mg-ions may have been depleted by precipitation should be only few meters thick (Le Deit et al., 2012; Loizeau et al., 2018), but not tens of meters, as observed in the study area. The lack of Fe/Mg-phyllosilicates might be attributable to limited available spectral data or imprecise measurements.

Differently polygonized layers L1 and L2 within lNlp might have their origin in changing environmental conditions with variable availability of water or changing temperatures (El-Maarry et al., 2010, 2014). The detected jarosite in layer L1 suggests the release of substantial amounts of sulphur-rich volatiles to the atmosphere. This could lead to the subsequent formation of sulfates as jarosite (Farrand et al., 2009). Eventual climate change to an environment with arid periods, consistent with jarosite as a water-limited weathering product (Elwood Madden et al., 2004) could have led to the polygonalization of unit lNlp by desiccation. Within the so interpreted desiccation cracks, jarosite accumulated and documents the change of the chemical environment, since jarosite forms in rather acidic environments (Papike et al., 2006).

4.1.2. Fluvial Systems

After the drainage of the Eridania paleolake at the end of Late Noachian (Irwin et al., 2002, 2004), the slightly lithified sediments were exposed to the atmosphere and were susceptible to erosion processes. Fluvial systems heading from the rim of Gorgonum Chaos toward its center could have eroded channels into the flat surface of the basin floor and thus into lNlp.

Incised valleys are distributed along the whole rim around Gorgonum Chaos (Howard & Moore, 2011). The water source for the fluvial systems was probably precipitation driven runoff, as described by Burr et al. (2009). This took place around the Noachian-Hesperian transition when the water level of the paleolake dropped but there was still a limited amount of liquid water on the surface. Another possible water source could be thawing ice from permafrost beneath the surface, which released meltwater during impact events or episodic volcanic activity. However, evidence for this hypothesis was not found in the study area. Feeding the rivers from groundwater seems unlikely, as the required reservoirs in the elevated basin rim seem to be too limited in their extent to store significant amounts of groundwater.

In the study area, the general direction of river channels from east to west correlates with the slope of the basin floor in this region of Gorgonum Chaos (Figure 9). The network type can be categorized as subparallel (Burr et al., 2009). In the east of the large depression, the mostly refilled southeastern crater may have served as a reservoir from which a fluvial system was fed through a gap in the northern crater wall (Figure 9). In the west of the large depression, channels are traceable at the flat basin floor. Inside the large depression, between the supposed reservoir and the channels, a number of sinuous ridges were observed.

The cross-sectional profiles of these ridges range between sharp-crested and flat-topped. The width of the ridges increases westwards and may reflect the longer duration that the east of the ridges was exposed to aeolian erosion. Therefore, the ridges are less wide in the east. Where the flat tops of the ridges are broad, narrow troughs are running along the trend of the inverted ridges and are identified as the original river channels. We interpret the sinuous ridges in the large depression of the study area as inverted paleochannels of a former fluvial system, as reported elsewhere on Mars (Davis et al., 2016; Lefort et al., 2012; Pain et al., 2007; Skinner et al., 2021).

We assume that at the end of the stage of fluvial erosion the availability of water decreased and minor amounts of water carried the sediments that refilled the channels. NHr is the result of this deposition and chloride salts detected in this unit indicate a transport of material mobilized by brines. The age of NHr cannot be determined exactly, but is limited between the underlying Late Noachian lNlp and the Late Hesperian, when evidence of sufficient surface water is still confirmed in this and other regions on Mars (Howard & Moore, 2011; Hynek et al., 2010; Mangold et al., 2004; Werner & Tanaka, 2011; Wendt et al., 2013). When the channels fell dry, the characteristic desiccation cracks emerged with their polygonal to blocky morphology (Goodall et al., 2000; El-Maarry et al., 2010, 2014; Pascuzzo et al., 2019). CRISM data and visual investigation suggest that the desiccation cracks were refilled with evaporitic chlorides when small amounts of liquid water were available again (Figures 4d–4f).

The morphological analyses reveal that NHr is more erosion-resistant than the directly underlying lNlp. This enhanced competence is either a consequence of the filling of cracks in NHr with coarse fluvial deposits or due to cementation of single sediment grains (Kerber et al., 2017). The chlorides from brines might work as cement and would be sufficient to enable this process, consistent with the notion of Williams et al. (2018) that fluvial channels on Mars are typically inverted due to cementation, as opposed to clast armoring or lava filling. A changed grain-size may also have an effect on the consolidation of the material, whereby larger grains increase the resistance to erosion. Briny water could have transported gravel or small

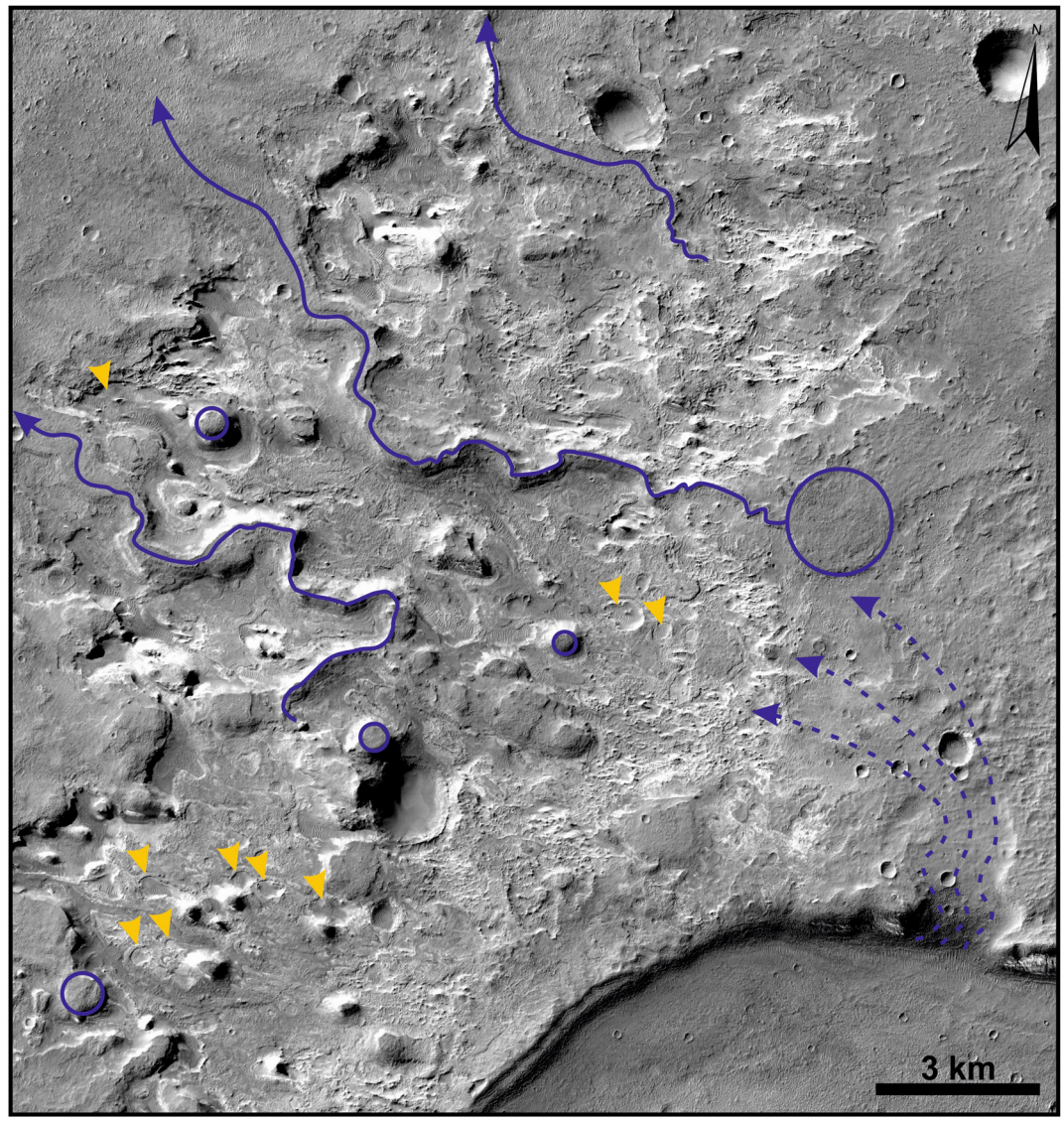

Figure 9. An enlarged section of the northern part of the large depression based on Context Camera (CTX) image J03_045766_1410 (6 m/pixel). Recognizable are sinuous ridges (solid blue lines), circular mounds (blue circles), several pits (yellow arrows), and a spillpoint in the northern crater wall with the assumed direction of flowing water (dashed blue lines).

rocks, which accumulated on the channel ground and caused an additional increase in grain-size and therefore the consolidation of the unit. This more consolidated unit protected the underlying lNlp from aeolian erosion (Burr et al., 2009), thus fluvial channels were exhumed and inverted into ridges. The increased relevance of wind erosion supports the inversion of features at numerous locations on Mars (Pain et al., 2007).

We interpret circular mounds or mesas within or at the rim of the large depression as inverted impact craters. As with the formation of inverted channels, filling of craters with sediments and their subsequent cementation with chlorides is most plausible. This is supported by the emergence of inverted channels at the western rim of some inverted craters (Figure 9). These craters probably were filled with water and streams started from their rims until the craters were refilled with salty sediments.

4.1.3. Glacial Systems?

Although glacial conditions have been predicted for the highlands at the late Noachian (Wordsworth et al., 2013) and recently some morphological evidence for glacial processes has been identified (e.g.,

Bouquety et al., 2019; Grau Galofre et al., 2020), we could not find any glacial landforms in the study area. However, it has been suggested that sulfate formation on Mars may have occurred under glacial conditions (Michalski & Niles, 2012), and recently it was indeed found that jarosite can be formed in deep ice on Earth (Baccolo et al., 2021). As the amounts of water to form the relatively small valleys in our study area may have been generated under a "late Noachian icy highland" scenario (Palumbo et al., 2018), we cannot exclude that the climatic conditions in our study area at the time after the drainage of the Eridania paleolake were dominated by an overall cold and dry climate.

We consider it unlikely that the observed sinuous ridges are eskers. Glacial eskers usually present longitudinal discontinuities in width and height and have a narrow and steep-sided morphology with sharp or rounded crests (Pain et al., 2007). In contrast, the observed sinuous ridges are continuously flat topped over several kilometers and are mostly wider than high. This is typical for inverted channels. The apparent absence of other evidence of glaciation in the study area also argues against a formation as eskers.

4.2. Aeolian Erosion and Deposition

4.2.1. Aeolian Erosion

The two depressions observed at the eastern flank of the basin are the result of erosion and degradation in this area. Additionally, the inverted features in the depressions are clear indications of an active erosional mechanism. Fluvial, glacial, or aeolian erosion may have been the formative process of both depressions: Fluvial erosion would require an extensive inflow of liquid water, which means the presence of valleys or inlet channels at the eastern side of the basin. This has, however, not been observed in this area. Additionally, the eroded material with liquid water had to be deposited at the downstream side of the basin. We have not found any evidence of large depositional features in the area.

The large depression most likely started to form at the rim of the southeastern crater. After the water of the paleolake receded, the southeastern crater wall was in an exposed position to the wind system compared to the basin floor. This may be an explanation why the crater rim was a preferred starting point for aeolian erosion. The observation of elongated buttes and parallel traces of aeolian erosion suggests winds from west-northwest during the erosion of the large depression. The wind eroded the flanks of the southeastern crater rim and created an erosion front that excavated westwards into unit lNlp. Variations in the unit's consolidation or superposing deposits of unit NHr reduced the erosion rate, because they may be more resistant against erosion. This caused the formation of terraces, and inverted morphologies. Where layer L1 started to erode, pits evolved through erosion of the weaker underlying material. At the western rim of the depression the abrasion was increased possibly by the emerged lee side and thus stronger aeolian turbulences (Pye & Tsoar, 2009). Parallel crests at the bottom of the pits could be lithified TARs or Periodic Bedrock Ridges (PBR) (Silvestro et al., 2021) which form in interaction with TARs and may differ somewhat from the dominating wind direction during this period. Their orientation is south-southwest to north-northeast, comparable to that of much younger TARs, and may indicate a local wind system that was stable during long periods of Gorgonum's history. Similar to L1, capping layer L2 prevented the underlying material from complete erosion. Due to its higher elevation and longer exposure to erosion, only detached buttes remained. The orientation of the slightly elongated buttes to west-east is a result of erosion caused by wind (Armstrong & Leovy, 2005; Golombek & Bridges, 2000) that constantly came from a western direction.

Buttes, pits, and TARs were found to a minor extent in the area of the smaller depression that is located directly adjacent to a wrinkle ridge. We interpret these morphological features as indicators for an equivalent origin of the smaller depression by aeolian erosion. The wrinkle ridge is part of an extended system of tectonic features that is related to the rise of the Tharsis region (Chicarro et al., 1985; Capitan & Van De Wiel, 2011; Mueller & Golombek, 2004). The wrinkle ridge was formed on the Gorgonum basin floor in the post-Noachian period (Carr & Head, 2010) after the final deposition of lNlp and NHlr (Wendt et al., 2013). This would constrain the age of the wrinkle ridge to the Middle to Late Hesperian. A local verification of this estimated age is not possible, due to the lack of datable units in the vicinity of the wrinkle ridge. After its folding and exposure to the erosional wind system, the wrinkle ridge may have acted as a starting point for the rapid abrasion of lNlp. Due to the development of the wrinkle ridge long after the basin was desiccated, there was less time to erode a more extended depression. Geomorphologically, both depressions in

the study area are deflation basins and were formed under similar initial conditions at an elevated crater rim or wrinkle ridge.

Global erosion rates decreased after the Noachian-Hesperian transition by 2–5 orders of magnitude (e.g., Golombek et al., 2014; Warner et al., 2020). Therefore, the incision of both depressions came largely to an end until the Late Hesperian. The decreased erosion rates during the Amazonian may have been capable of removing weakly consolidated air fall material locally, but were not sufficient to deepen the depressions substantially.

4.2.2. Aeolian Deposition of NHlr

Based on our HiRISE observations, NHlr is predominantly unstructured (Figure 4g) and susceptible to erosion processes that modified its morphology. This leads to the assumption that NHlr is only slightly lithified. A material of similar appearance was found and classified as loess-like by Grant and Schultz (1990) and was named "Electris deposit." They also found that the material is depleted in hydrated minerals. Abundant amounts of Electris deposits were found in the region of Sirenum Fossae, interpreted as aeolian deposits, and dated to middle to late Hesperian (Grant & Schultz, 1990; Grant et al., 2010). However, despite the interpretation as aeolian material, deposition from volcanic ash airfall cannot be ruled out (de Pablo et al., 2005). We conclude that NHlr is an equivalent unit and its age can be derived more precisely as compared to the relative age approximation in relation to older units lNlp and NHr. In the east of the study area the thickness of NHlr cannot be estimated and might exceed tens to hundreds of meters. This would be consistent with Electris deposits observed in Eridania basin (Adeli et al., 2015) and in the center of Gorgonum Chaos in particular (Wendt et al., 2013). The appearance of the unit within the large depression and the absence of it in the small depression implies that it was either deposited between the formation of both depressions or the unit was completely removed from the small depression. The lack of absorption bands in the spectral ratio BD1900R (Viviano-Beck et al., 2014) excludes the presence of considerable amounts of hydrated minerals in NHlr. This suggests that the formation of the unit was not affected by liquid water. The option of an impact ejecta origin of NHlr, suggested by its vicinity to the rim of the southeastern crater, can be rejected due to the absence of hydrated minerals. An impact younger than lNlp would produce ejecta from the underlying unit lNlp, which presents distinct signs of hydration. If the crater and its ejecta are older than the hydrated basin unit lNlp, ejected material would not drape younger lNlp, which NHlr does.

4.2.3. Deposition of Air Fall

Based on our results of the model age determination, unit Adc was most likely deposited during the early to middle Amazonian (see Section 3.2, Figure 5). In a region of possible volcanic activity, 200 km southwest of the study area, Brož et al. (2015) identified volcanic domes and cones with a model age between 660 Ma (±100 Ma) and 470 Ma (±100 Ma). The surface-age of the southeastern crater filling is comparable to the age of these volcanic activities, taking into account the varying result of the deposition model ages for this unit in the study area. Unit Adc contains ultramafic magnesium-rich olivine and calcium-rich pyroxene and lacks hydrated minerals such as phyllosilicates (Figure 7c). This olivine-rich material was exposed to the surface over extended time periods, which indicates the absence of water and thus arid climate conditions during and after its deposition. Otherwise, the presence of water would have led to rapid chemical alteration of olivine into secondary minerals (Bach et al., 2006). Lateral extent, homogeneous thickness, age, and mineralogy of unit Adc make an interpretation as volcanic material plausible, which might have been deposited by air fall. The characteristics of Adc are similar to the dark mantling in Mawrth Valles described by Loizeau et al. (2007, 2010, 2018) and Kremer et al. (2018). The spectral analyses presented in these studies also report pyroxene-rich materials and support the results of our study.

The orientation of elongated deposits of Adc at the bottom of depressions is consistent with those of TARs or elongated pits in the study area. They were interpreted as a result of aeolian erosion by constant wind from west-northwest to east-southeast. Inside the depressions, almost the entire unit was removed except some local remains. Adc directly drapes lNlp, but was sparsely found on top of NHlr. This might be explained by the minor solidification of NHlr on whose weak and rugged surface a firm coverage of Adc could not form, because both units were preferentially transported away by abrasion.

The density of olivine (4.3 g/cm^3, Deer et al., 1992) is significantly higher than the density of pyroxene (3.6 g/cm^3, Deer et al., 1992). Exposed to constant wind, the pyroxene could have been transported away

more easily, while olivine remains on top of the basin floor (Mangold et al., 2011). In return, the pyroxene could accumulate at the lee sites within the two depressions and causes the darker appearance of the accumulated material. Therefore, the albedo variations of the subunits of Adc could be explained by wind-driven separation caused by different mineral densities.

Large quantities of unconsolidated unit Al, originating from Adc, suggest a susceptibility of the cap to abrasion. Therefore, the notion that unit Adc appears moderately solidified based on the observation of occasionally shed boulders, could be misleading. Despite the very thin Amazonian atmosphere this material formed TARs with similar albedo as Adc. The orientation of the TARs indicates a constant wind direction from west-northwest. A targeted spectral analysis was not possible, but where extended areas of TARs occur, THEMIS DCS 8-7-5 data are characterized by purple and green signatures, suggesting olivine and pyroxene, respectively. This is because the majority of the TARs are formed directly on Adc or in the immediate vicinity of this unit. The ripples of subunit Abc appear slightly lighter than the superimposed unit Adc. In addition to the described mineral segregation, it is conceivable that the ripple-covered surface of Abc causes an improved capability of oriented reflection of sunlight. This would be supported by the generally north-south striking ripples or TARs (see Figure 4i) in combination with almost 70° solar incidence angles of the CTX images. The surface of Adc without ripples or TARs could lead to a rather diffuse light scattering and thus a darker appearance.

4.3. Chronology of Surface Modification

Based on our geomorphological observations, spectral analyses and the stratigraphical relation between geological units, we were able to reconstruct the geological history of the study area (Figure 10). This includes interpretations of the absolute model age of deposition of the geological units, the environmental conditions during their formation and the formative processes, which led to the resurfacing phases.

Large basins on Mars are commonly filled with extrusive magmas to a horizontal level (Irwin et al., 2004). In contrast, the bowl-shaped topography of Gorgonum Chaos is untypical for basins of this size. The oldest observed unit lNlp (Figure 8b) at the basin floor was probably formed as an air fall deposit (Grant et al., 2010; Wendt et al., 2013) that sunk down to the ground of the hypothesized Noachian Eridania paleolake system before 3.7 Ga (Irwin et al., 2002, 2004) (Figure 10). The sedimentation of this aeolian transported material led to deposits of approximately constant thickness resulting in the bowl-shaped topography of the basin. Scarps around the −300 m and −50 m contour lines of Gorgonum Chaos suggest an ice-cover of the hypothesized paleolake (Howard & Moore, 2004). However, these features are located outside the study area and we do not see evidence of past ice cover in our region.

The drainage of the Eridania paleolake through Ma'adim Vallis started around the Noachian-Hesperian transition 3.73 Ga (+0.07/−0.15 Ga) ago (Irwin et al., 2002, 2004). Resurfacing processes started immediately after the paleolake fell dry and the former lake floor deposits were exposed to surface conditions. Impacts started to form craters and fluvial systems incised valleys into the weak basin floor sediments, driven by precipitation or episodic melting events (Craddock & Howard, 2002; Wordsworth, 2016) (Figure 10). A possible source reservoir for liquid water of the fluvial systems could be the crater in the southeast of the study area. It is almost completely filled with sediments that might originate from adjacent southern highlands. The gap in the northern rim of the southeastern crater (Figure 9) could have been a spill-over point and is morphologically reminiscent of an outflow channel from which water could have fed the fluvial systems. North of the study area, other inverted channels were found with dimensions and orientation very similar to those in the study area. This implies that the southeastern crater was only a local reservoir for spatially limited river systems, since more distant rivers could not have been fed from the southeastern crater. The generally similar appearance of inverted channels within and outside the study area makes a common origin plausible.

As the availability of surface water decreased in the Hesperian, the valleys and craters were refilled with late-stage fluvial sediments, transported by brines. Evaporitic chloride salts from these briny solutions filled the space of desiccation cracks and cemented the newly formed sediments within fluvial valleys and craters to unit NHr (Goodall et al., 2000). Due to this cementation, unit NHr is more solidified compared to underlying lNlp. Subsequent aeolian erosion reshaped the basin floor, preferential at wind-exposed morphologies.

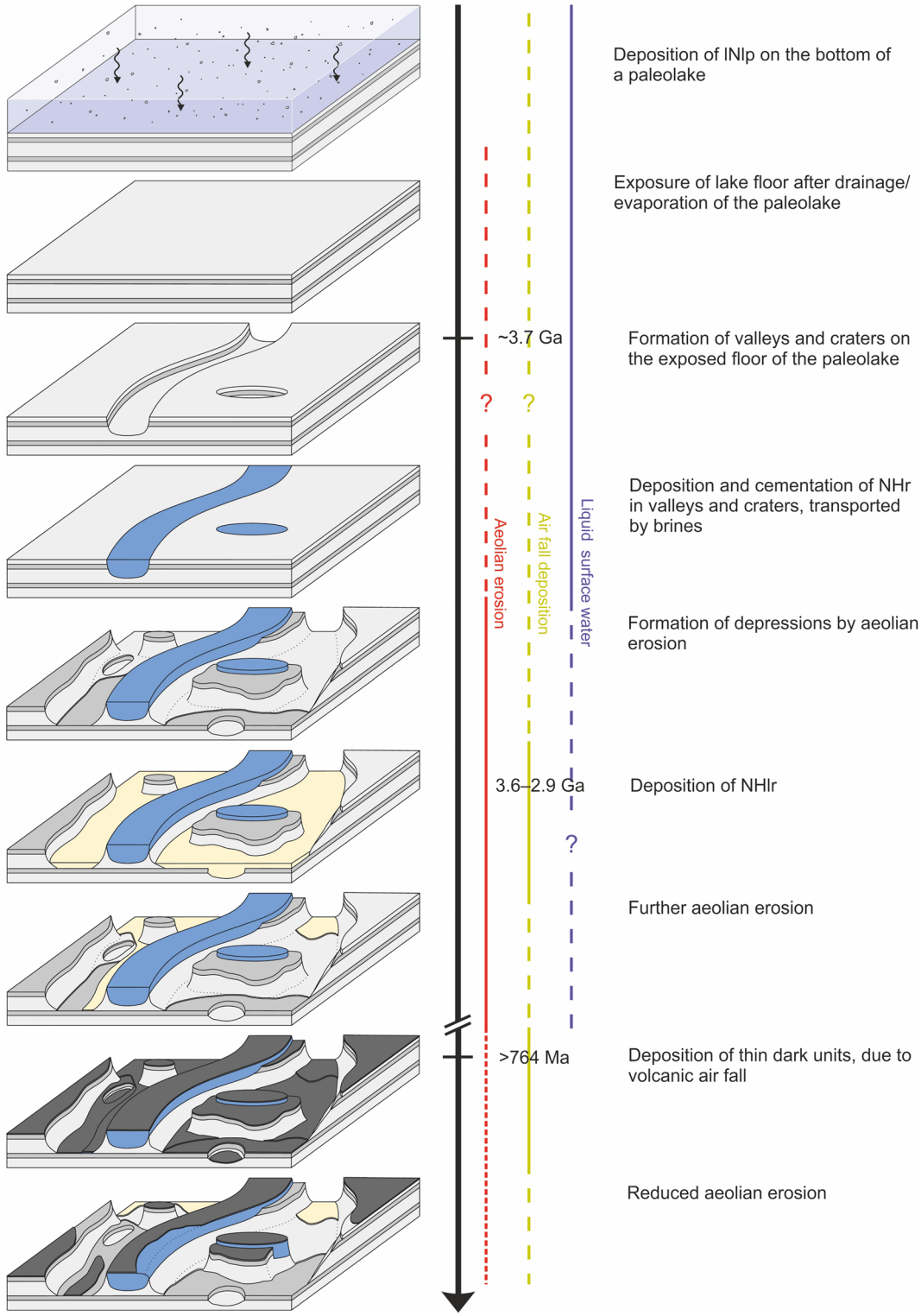

Figure 10. Interpreted chronology of deposition and erosion with associated model ages in southeastern Gorgonum Chaos. The color scheme of the units is consistent with the legend in Figure 3. Distinctly polygonized layers within unit lNlp are indicated in medium gray.

In the study area the aeolian erosion started at the western rim of the southeastern crater and formed the large depression. The orientation of the long axis of the depression if likely controlled by NE-trending ancient extensional basins and ranges that formed in the early Noachian (Anderson et al., 2019). Later, during Hesperian tectonics (Chicarro et al., 1985; Baker & Head, 2009; Mueller & Golombek, 2004; Wilson & Head, 2002), a wrinkle ridge was formed in the northwest of the study area. This ridge started to erode and the small depression evolved. Due to the increased consolidation of NHr and of layers L1 and L2 within lNlp, extensive abrasion of underlying material was prevented. This resulted in the development of inverted landforms, terraces, and local pits within the depressions (Figure 10).

Until the Late Hesperian the depressions were partly refilled with NHlr (Figure 9) that is reminiscent of loess-like Electris deposits (Grant et al., 2010). Due to the reduced competence of NHlr, it is more susceptible to abrasion and was eroded faster than older units. After the removal of NHlr from major parts of the large depression, possibly previously buried TARs or PBRs were exhumed again or PBRs formed after exposure of lNlp. The lithification of TARs and the PBRs are evidenced by their polygonized appearance and enhanced resistance to subsequent erosion. Their orientation is the same as of the younger and possibly active TARs and indicates a west-northwest to east-southeast wind direction. From Early to Late Hesperian aeolian erosion rates decreased dramatically and the growth of the depressions came to an end.

During the Amazonian until ~764 Ma (±200 Ma) ago Adc was formed of mafic (olivine- and pyroxene-rich) air fall material under dry conditions. The material of this unit is of volcanic origin (Kremer et al., 2018; Loizeau et al., 2010, 2018) and uniformly drapes the study area. Subsequently, large amounts of Adc, especially in the depressions, were eroded by wind and redeposited as subunits Abc, At and Al (Bourke et al., 2010).

The layered appearance of youngest unit lAs at south-facing slopes is explainable by periodic deposition and preservation. In more flat areas the unit seems to be removed after every phase of deposition. The white color and the occurrence of lAs at latitude between 30–50° leads to a classification of the unit as latitude dependent mantle (LDM). LDM is ubiquitous at these latitudes on Mars and forms as a layered dust-ice mixture in the course of obliquity changes of the Martian spin axis and related climate changes (see review by Forget et al., 2017, and references therein). LDM is not older than 10 Ma (Mustard et al., 2001; Kreslavsky & Head, 2002; Willmes et al., 2012). Distinct layers within the unit might represent different periods of obliquity change. These are preserved at pole-facing slopes, in contrast to sun-exposed areas where the unit decayed at the end of an obliquity change cycle.

4.4. Context Within Eridania Basin

Despite the large spatial extent of the Eridania basin and its division into sub-basins, a number of similarities between these individual sub-basins could be observed. The most striking is the presence of thick deposits rich in phyllosilicates, indicating the presence of liquid water in the early history of Mars (Adeli et al., 2015; Golder & Gilmore, 2013; Leask et al., 2017). Another common characteristic of the deep centers of the sub-basins, such as Ariadnes Colles, Atlantis Chaos, or Gorgonum Chaos, is the presence of deposits enriched in sulfates and their decreasing concentration toward the basin rims. On the other hand, the amount of chlorides increases toward the shallow rims (Leask et al., 2019; Michalski et al., 2017). This trend can be confirmed in our study area, since chlorides could be detected comparatively frequently and sulfates only occasionally. The origin of these minerals cannot be conclusively determined in the study area. Due to its marginal position within the basin no traces of possible hydrothermal processes could be observed, as the latter are hypothesized for the deep regions of the basins, where they could have transported sulfates from the crust to the lake sediments (Michalski et al., 2017).

Our suggestion that the liquid water in the paleolake may originate partly from episodically melting ice reservoirs is also consistent with observations from other regions of Gorgonum Chaos and the surrounding areas (Capitan & Van De Wiel, 2010; Márquez et al., 2005). Volcanism could repeatedly thaw ice-rich deposits and provide replenishment of groundwater reservoirs and subsequent water influx into Eridania basin.

5. Conclusions

1. We produced a geological map of southeastern Gorgonum Chaos, which includes major morphological features and five geological units with model ages ranging from Late Noachian to Late Amazonian. Stratigraphic and spectral analyses reveal a very diverse mineralogy, which has evolved during Martian history.
2. Gorgonum Chaos hosted a lake, which was drained or desiccated ~3.7 Ga ago. During the existence of this paleolake air fall material was deposited at the basin floor and formed a unit of light-toned material that is enriched in kaolinite and is at least 200 m thick. The eventual desiccation of the lake during the climate change to more arid and acidic environments led to polygonization of the basin unit and its enrichment in jarosite. Channels and craters were incised into the surface by rivers and impactors and were filled with liquid water. The hydrated minerals, kaolinite and jarosite, and fluvial erosion indicate an active hydrologic system, which was still active after drainage and desiccation of Gorgonum Chaos.
3. The Hesperian was characterized by alternating phases of sedimentation and aeolian erosion. Fluvial valleys and craters were refilled with sediments around the Noachian-Hesperian transition and chloride-rich salts from brines cemented the filling. Subsequent abrasion formed depressions at the surface of the basin floor. During this process, the refilled channels and craters were exposed and preserved as inverted morphological features. Subsequently, the depressions were refilled with loess-like material and were partly excavated again. Low amounts of hydrated minerals in this loess-like material indicate predominantly arid conditions in Gorgonum Chaos during this period.
4. Episodes of Amazonian volcanic activity in the region of Eridania basin sourced the thin deposited layer of air fall materials composed of olivine and pyroxene. The stability of olivine under ultra-arid conditions suggests the complete loss of surface water around the Hesperian-Amazonian transition.
5. The duration of water sustaining conditions in the geological history of Gorgonum Chaos remains uncertain, but could be improved by further age determinations by crater counting. This would inform the question of how long the fluvial systems were active after the desiccation of the lake and constrain the period in which the depressions were formed by abrasion.
6. Morphology and mineralogy in southeastern Gorgonum Chaos document phases of climate change from a humid and alkaline/neutral environment at the end of the Noachian, through arid and more acidic environments in the Hesperian to the ultra-arid conditions in the Amazonian, which we still observe on Mars today.

Data Availability Statement

IDs of imagery, spectroscopic, and topographic datasets to support this paper are listed below and can be found in the Mars Image Explorer (http://viewer.mars.asu.edu/): *CTX* (J03_045766_1410, J03_045977_1395), *HiRISE* (ESP_019261_1410, ESP_045977_1405, ESP_047546_1410, ESP_048469_1410, ESP_048614_1410, ESP_048825_1410, ESP_050526_1410), *CRISM* (FRS0003BCB2, FRS0003C079), *THEMIS* (*Day/DCS 8-7-5*: I33652003, I41776002; *Night*: I02684006, I07902021), *HRSC* (H2575_0000). The laboratory spectra are found in the USGS Digital Spectral Library (https://www.usgs.gov/labs/spec-lab/capabilities/spectral-library). All created data as shape files, DEMs, etc. are available at Haack, D (2021). Southern Gorgonum Chaos-ArcGis. Figshare. https://doi.org/10.6084/m9.figshare.15144285.

Acknowledgments
The authors thank Lida Fanara for her valuable help in creating the high-resolution DTMs. Open access funding enabled and organized by Projekt DEAL.

References

Adeli, S., Hauber, E., Le Deit, L., & Jaumann, R. (2015). Geologic evolution of the eastern Eridania basin: Implications for aqueous processes in the southern highlands of Mars. *Journal of Geophysical Research: Planets*, *120*, 1774–1799. https://doi.org/10.1002/2015je004898

Alemanno, G., Orofino, V., & Mancarella, F. (2018). Global map of Martian fluvial systems: Age and total eroded volume estimations. *Earth and Space Science*, *5*, 560–577. https://doi.org/10.1029/2018ea000362

Anderson, R. C., Dohm, J. M., Williams, J. P., Robbins, S. J., Siwabessy, A., Golombek, M. P., & Schroeder, J. F. (2019). Unraveling the geologic and tectonic history of the Memnonia-Sirenum region of Mars: Implications on the early formation of the Tharsis rise. *Icarus*, *332*, 132–150. https://doi.org/10.1016/j.icarus.2019.06.010

Armstrong, J. C., & Leovy, C. B. (2005). Long term wind erosion on Mars. *Icarus*, *176*, 57–74. https://doi.org/10.1016/j.icarus.2005.01.005

Baccolo, G., Delmonte, B., Niles, P. B., Cibin, G., Stefano, E. D., Hampai, D., et al. (2021). Jarosite formation in deep Antarctic ice provides a window into acidic, water-limited weathering on Mars. *Nature Communications*, *12*, 436. https://doi.org/10.1038/s41467-020-20705-z

Bach, W., Paulick, H., Garrido, C. J., Benoit Ildefonse, B., Meurer, W. P., & Humphris, S. E. (2006). Unraveling the sequence of serpentinization reactions: Petrography, mineral chemistry, and petrophysics of serpentinites from MAR 15°N (ODP Leg 209, Site 1274). *Geophysical Research Letters*, *33*, L13306. https://doi.org/10.1029/2006GL025681

Baker, D. M., & Head, J. W. (2009). *The origin of Eridania Lake and Ma'adim Vallis: An investigation of closed Chaos basins, Hesperian ridged plains, and tectonic constructs on the floor of a large hypothesized paleolake on Mars*. Lunar and planetary science conference. The Woodlands, TX, USA.

Balme, M., Berman, D. C., Bourke, M. C., & Zimbelman, J. R. (2008). Transverse aeolian ridges (TARs) on Mars. *Geomorphology*, *101*(4), 703–720. https://doi.org/10.1016/j.geomorph.2008.03.011

Bibring, J. P., Langevin, Y., Mustard, J. F., Poulet, F., Arvidson, R., Gendrin, A., et al. (2006). Global mineralogical and aqueous Mars history derived from OMEGA/Mars Express data. *Science*, *312*, 400–404. https://doi.org/10.1126/science.1122659

Bishop, J. L., Dyar, M. D., & Brown, A. J. (2008). Reflectance and emission spectroscopy study of four groups of phyllosilicates: Smectites, kaolinite-serpentines, chlorites and micas. *Clay Minerals*, *43*(1), 35–54. https://doi.org/10.1180/claymin.2008.043.1.03

Bishop, J. L., Pieters, C. M., Burns, R. G., Edwards, J. O., Mancinelli, R. L., & Froeschl, H. (1995). Reflectance spectroscopy of ferric sulfate-bearing montmorillonites as Mars soil analog materials. *Icarus*, *117*, 101–119. https://doi.org/10.1006/icar.1995.1145

Bouquety, A., Sejourné, A., Costard, F., Mercier, D., & Bouley, S. (2019). Morphometric evidence of 3.6 Ga glacial valleys and glacial cirques in Martian highlands: South of Terra Sabaea. *Geomorphology*, *334*, 91–111. https://doi.org/10.1016/j.geomorph.2019.02.022

Bourke, M. C., Lancaster, N., Fenton, L. K., Parteli, E. J. R., Zimbelman, J. R., & Radebaugh, J. (2010). Extraterrestrial dunes: An introduction to the special issue on planetary dune systems. *Geomorphology*, *121*(1–2), 1–14. https://doi.org/10.1016/j.geomorph.2010.04.007

Brož, P., Hauber, E., Platz, T., & Balme, M. (2015). Evidence for Amazonian highly viscous lavas in the southern highlands on Mars. *Earth and Planetary Science Letters*, *415*, 200–212. https://doi.org/10.1016/j.epsl.2015.01.033

Burns, R. G. (1993). *Mineralogical applications of crystal field theory*. New York, NY: Cambridge University Press.

Burr, D. M., Enga, M.-T., Williams, R. M. E., Zimbelman, J. R., Howard, A. D., & Brennand, T. A. (2009). Pervasive aqueous paleoflow features in the Aeolis/Zephyria Plana region, Mars. *Icarus*, *200*, 52–76. https://doi.org/10.1016/j.icarus.2008.10.014

Capitan, R. D., & Van De Wiel, M. (2011). Landform hierarchy and evolution in Gorgonum and Atlantis basins, Mars. *Icarus*, *211*(1), 366–388. https://doi.org/10.1016/j.icarus.2010.08.006

Carr, M. H., & Head, J. W. (2010). Geologic history of Mars. *Earth and Planetary Science Letters*, *294*, 185–203. https://doi.org/10.1016/j.epsl.2009.06.042

Carter, J., Loizeau, D., Mangold, N., Poulet, F., & Bibring, J. P. (2015). Widespread surface weathering on early Mars: A case for a warmer and wetter climate. *Icarus*, *248*, 373–382. https://doi.org/10.1016/j.icarus.2014.11.011

Chaves, L. C., Horgan, B., Lynch, K. L., Kimbrough, L., Hanley, J., & Wray, J. J. (2018). *Acidic environments in columbus crater, Mars: Implications for habitability. 49th lunar and planetary science conference (No. 2083)*.

Chicarro, A. F., Schultz, P. H., & Masson, P. (1985). Global and regional ridge patterns on Mars. *Icarus*, *63*(1), 153–174. https://doi.org/10.1016/0019-1035(85)90025-9

Christensen, P. R., Jakosky, B. M., Kieffer, H. H., Malin, M. C., Mcsween, H. Y. Jr, Nealson, K., et al. (2004). The Thermal Emission Imaging System (THEMIS) for the Mars 2001 Odyssey Mission. *Space Science Reviews*, *110*, 85–130. https://doi.org/10.1007/978-0-306-48600-5_3

Clark, R. N., King, T. V. V., Klejwa, M., Swayze, G. A., & Vergo, N. (1990). High spectral resolution reflectance spectroscopy of minerals. *Journal of Geophysical Research*, *95*(B8), 12653–12680. https://doi.org/10.1029/JB095iB08p12653

Clark, R. N., Swayze, G. A., Wise, R., Livo, E., Hoefen, T., Kokaly, R., & Sutley, S. J. (2007). *USGS digital spectral library Splib06a: U.S. Geological Survey, digital data series 231*. Denver, CO: U.S. Geological Survey.

Cloutis, E. A., Hawthorne, F. C., Mertzman, S. A., Krenn, K., Craig, M. A., Marcino, D., et al. (2006). Detection and discrimination of sulfate minerals using reflectance spectroscopy. *Icarus*, *184*(1), 121–157. https://doi.org/10.1016/j.icarus.2006.04.003

Craddock, R. A., & Howard, A. D. (2002). The case for rainfall on a warm, wet early Mars. *Journal of Geophysical Research*, *107*, 5111. https://doi.org/10.1029/2001JE001505

Davila, A. F., Gross, C., Marzo, G. A., Fairen, A. G., Kneissl, T., McKay, C. P., & Dohm, J. (2011). A large sedimentary basin in the Terra Sirenum region of the southern highlands of Mars. *Icarus*, *212*(2), 579–589. https://doi.org/10.1016/j.icarus.2010.12.023

Davis, J. M., Balme, P. M., Grindrod, R. M. E., Williams, S., & Gupta (2016). Extensive Noachian fluvial systems in Arabia Terra: Implications for early Martian climate. *Geology*, *10*, 847–850. https://doi.org/10.1130/G38247.1

de Pablo, M. A., Márquez, A., Centeno, J. D., & Stansberry, E. (2005). Geomorphologic Map of the Atlantis Basin, Terra Sirenum, Mars. In S. Maxwell, & E. Stansbery (Eds.), *36th annual lunar and planetary science conference* (p. 1297).

Deer, W. A., Howie, R. A., & Zussman, J. (1992). *An introduction to the rock-forming minerals* (2nd ed., p. 698). New York, NY: Longman-Group Ltd.

El Maarry, M. R., Markiewicz, W. J., Mellon, M. T., Goetz, W., Dohm, J. M., & Pack, A. (2010). Crater floor polygons: Desiccation patterns of ancient lakes on Mars? *Icarus*, *115*. https://doi.org/10.1029/2010JE003609

El-Maarry, M. R., Watters, W., & McKeown, N. K. (2014). Potential desiccation cracks on Mars: A synthesis from modeling, analogue-field studies, and global observations. *Icarus*, *241*, 248–268. https://doi.org/10.1016/j.icarus.2014.06.033

Elwood Madden, M., Bodnar, R., & Rimstidt, J. (2004). Jarosite as an indicator of water-limited chemical weathering on Mars. *Nature*, *431*, 821–823. https://doi.org/10.1038/nature02971

Farrand, W. H., Glotch, T. D., Rice, J. W., Jr, Hurowitz, J. A., & Swayze, G. A. (2009). Discovery of jarosite within the Mawrth Vallis region of Mars: Implications for the geologic history of the region. *Icarus*, *204*(2), 478–488. https://doi.org/10.1016/j.icarus.2009.07.014

Fergason, R. L., Christensen, P. R., & Kieffer, H. H. (2006). High-resolution thermal inertia derived from the Thermal Emission Imaging System (THEMIS): Thermal model and applications. *Journal of Geophysical Research*, *111*. https://doi.org/10.1029/2006JE002735

Forget, F., Byrne, S., Head, J. W., Mischna, M. A., & Schörghofer, N. (2017). Recent climate variations. In R. M. Haberle, R. T. Clancy, F. Forget (Eds.), *The atmosphere and climate of Mars* (pp. 497–525). Cambridge University Press. https://doi.org/10.1017/9781139060172.016

Gillespie, A. R., Kahle, A. B., & Walker, R. E. (1986). Color enhancement of highly correlated images. I. Decorrelation and HSI contrast stretches. *Remote Sensing of Environment*, *20*(3), 209–235. https://doi.org/10.1016/0034-4257(86)90044-1

Glotch, T. D., Bandfield, J. L., Tornabene, L. L., Jensen, H. B., & Seelos, F. P. (2010). Distribution and formation of chlorides and phyllosilicates in Terra Sirenum, Mars. *Geophysical Research Letters*, *37*, L16202. https://doi.org/10.1029/2010GL044557

Golder, K. B., & Gilmore, M. S. (2013). *Eridania Basin, Mars: Evolution of electris terrain, chaos, and paleolake. 44th lunar and planetary science conference. No. 2995*.

Golombek, M. P., Anderson, F. S., & Zuber, M. T. (2001). Martian wrinkle ridge topography: Evidence for subsurface faults from MOLA. *Journal of Geophysical Research*, *106*(E10), 23811–23821. https://doi.org/10.1029/2000JE001308

Golombek, M. P., & Bridges, N. T. (2000). Erosion rates on Mars and implications for climate change: Constraints from the Pathfinder landing site. *Journal of Geophysical Research*, *105*, 1841–1854. https://doi.org/10.1029/1999JE001043

Golombek, M. P., Warner, N. H., Ganti, V., Lamb, M. P., Parker, T. J., Fergason, R. L., & Sullivan, R. (2014). Small crater modification on Meridiani Planum and implications for erosion rates and climate change on Mars. *Journal of Geophysical Research: Planets*, *119*, 2522–2547. https://doi.org/10.1002/2014JE004658

Goodall, T. M., North, C. P., & Glennie, K. W. (2000). Surface and subsurface sedimentary structures produced by salt crusts. *Sedimentology*, *47*, 99–118. https://doi.org/10.1046/j.1365-3091.2000.00279.x

Grant, J. A., & Schultz, P. H. (1990). Gradational epochs on Mars: Evidence from west-northwest of Isidis Basin and Electris. *Icarus*, *84*, 166–195. https://doi.org/10.1016/0019-1035(90)90164-5

Grant, J. A., Wilson, S. A., Noe Dobrea, E., Fergason, R. L., Griffes, J. L., Moore, J. M., & Howard, A. D. (2010). HiRISE views enigmatic deposits in the Sirenum Fossae region of Mars. *Icarus*, *205*(1), 53–63. https://doi.org/10.1016/j.icarus.2009.04.009

Grau Galofre, A., Jellinek, A. M., & Osinski, G. R. (2020). Valley formation on early Mars by subglacial and fluvial erosion. *Nature Geoscience*, *13*, 663–668. https://doi.org/10.1038/s41561-020-0618-x

Grotzinger, J. P., Arvidson, R. E., Bell, J. F., Calvin, W., Clark, B. C., Fike, D. A., et al. (2005). Stratigraphy and sedimentology of a dry to wet eolian depositional system, Burns formation, Meridiani Planum, Mars. *Earth and Planetary Science Letters*, *240*(1), 11–72. https://doi.org/10.1016/j.epsl.2005.09.039

Gwinner, K., Jaumann, R., Hauber, E., Hoffmann, H., Heipke, C., Oberst, J., et al. (2016). The High Resolution Stereo Camera (HRSC) of Mars Express and its approach to science analysis and mapping for Mars and its satellites. *Planetary and Space Science*, *126*, 93–138. https://doi.org/10.1016/j.pss.2016.02.014

Hartmann, W. K., & Neukum, G. (2001). Cratering chronology and the evolution of Mars. In R. Kallenbach, J. Geiss, & W. K. Hartmann (Eds.), *Chronology and evolution of Mars. Space sciences series of ISSI*. Dordrecht: Springer. https://doi.org/10.1007/978-94-017-1035-0_6

Howard, A. D., & Moore, J. M. (2004). Scarp-bounded benches in Gorgonum Chaos, Mars: Formed beneath an ice-covered lake? *Geophysical Research Letters*, *31*(1), L01702. https://doi.org/10.1029/2003GL018925

Howard, A. D., & Moore, J. M. (2011). Late Hesperian to early Amazonian midlatitude martian valleys: Evidence from Newton and Gorgonum basins. *Journal of Geophysical Research*, *116*(E5), E05003. https://doi.org/10.1029/2010JE003782

Hurowitz, J., Fischer, W., Tosca, N., Milliken, R. E. (2010). Origin of acidic surface waters and the evolution of atmospheric chemistry on early Mars. *Nature Geoscience*, *3*, 323–326. https://doi.org/10.1038/ngeo831

Hynek, B. M., Beach, M., & Hoke, M. R. T. (2010). Updated global map of Martian valley networks and implications for climate and hydrologic processes. *Journal of Geophysical Research*, *115*. https://doi.org/10.1029/2009JE003548

Irwin, R. P., Howard, A. D., & Maxwell, T. A. (2004). Geomorphology of Ma'adim Vallis, Mars, and associated paleolake basins. *Journal of Geophysical Research*, *109*, E12009. https://doi.org/10.1029/2004je002287

Irwin, R. P., Maxwell, T. A., Howard, A. D., Craddock, R. A., & Leverington, D. W. (2002). A large paleolake basin at the head of Ma'adim Vallis, Mars. *Science*, *296*, 2209–2212. https://doi.org/10.1126/science.1071143

Ivanov, B. A. (2001). Mars/moon cratering rate ratio estimates. *Space Science Reviews*, *96*, 87–104. https://doi.org/10.1023/A:1011941121102

Jakosky, B. M. (2021). Atmospheric loss to space and the history of water on Mars. *Annual Review of Earth and Planetary Sciences*, *49*, 71–93. https://doi.org/10.1146/annurev-earth-062420-052845

Kaplan, H. H., Milliken, R. E., Fernández-Remolar, D., Amils, R., Robertson, K., & Knoll, A. H. (2016). Orbital evidence for clay and acidic sulfate assemblages on Mars based on mineralogical analogs from Rio Tinto, Spain. *Icarus*, *275*, 45–64. https://doi.org/10.1016/j.icarus.2016.03.019

Kerber, L., Dickson, J. L., Head, J. W., & Grosfils, E. B. (2017). Polygonal ridge networks on Mars: Diversity of morphologies and the special case of the Eastern Medusae Fossae Formation. *Icarus*, *281*, 200–219. https://doi.org/10.1016/j.icarus.2016.08.020

Kneissl, T., van Gasselt, S., & Neukum, G. (2011). Map-projection-independent crater size frequency determination in GIS environments: New software tool for ArcGIS. *Planetary and Space Science*, *59*, 1243–1254. https://doi.org/10.1016/j.pss.2010.03.015

Kremer, C. H., Mustard, J. F., & Bramble, M. S. (2018). *Origin and emplacement of the Circum-Isidis olivine-rich unit. 49th lunar and planetary science conference. LPI Contrib. No. 2083. id.1545.*

Kreslavsky, M. A., & Head, J. W. (2002). Mars: Nature and evolution of young latitude-dependent water-ice-rich mantle. *Geophysical Research Letters*, *29*. https://doi.org/10.1029/2002GL015392

Le Deit, L., Flahaut, J., Quantin, C., Hauber, E., Mège, D., Bourgeois, O., et al. (2012). Extensive surface pedogenic alteration of the Martian Noachian crust suggested by plateau phyllosilicates around Valles Marineris. *Journal of Geophysical Research*, *117*. https://doi.org/10.1029/2011JE003983

Leask, E. K., Ehlmann, B. L., & Dundar, M. M. (2019). *Evidence for chemically distinct waters forming sulphates and chlorides in Terra Sirenum, Mars. 50th lunar and planetary science conference. No. 2636.*

Leask, E. K., Ehlmann, B. L., Wray, J. J., & Anderson, R. (2017). *Martian lake plumbing: Mineralogy, morphology, and geologic context of hydrated minerals in Terra Sirenum*. 48th lunar and planetary science conference No. 2609.

Lefort, A., Burr, D. M., Beyer, R. A., & Howard, A. D. (2012). Inverted fluvial features in the Aeolis-Zephyria Plana, western Medusae Fossae Formation, Mars: Evidence for post-formation modification. *Journal of Geophysical Research*, *117*, E03007. https://doi.org/10.1029/2011JE004008

Loizeau, D., Mangold, N., Poulet, F., Ansan, V., Hauber, E., Bibring, J.-P., et al. (2010). Stratigraphy in the Mawrth Vallis region through OMEGA, HRSC color imagery and DTM. *Icarus*, *205*(2), 396–418. https://doi.org/10.1016/j.icarus.2009.04.018

Loizeau, D., Mangold, N., Poulet, F., Bibring, J.-P., Gendrin, A., Ansan, V., et al. (2007). Phyllosilicates in the Mawrth Vallis region of Mars. *Journal of Geophysical Research*, *112*(E8). https://doi.org/10.1029/2006JE002877

Loizeau, D., Quantin, C., Carter, J., Flahaut, J., Thollot, P., Lozac'h, L., & Millot, C. (2018). Quantifying widespread aqueous surface weathering on Mars: The plateaus south of Coprates Chasma. *Icarus*, *302*, 451–469. https://doi.org/10.1016/j.icarus.2017.11.002

Malin, M. C., Bell, J. F., III, Cantor, B. A., Caplinger, M. A., Calvin, W. M., et al. (2007). Context camera investigation on board the Mars reconnaissance orbiter. *Journal of Geophysical Research*, *112*(E5), E05S04. https://doi.org/10.1029/2006je002808

Mangold, N., Baratoux, D., Arnalds, O., Bardintzeff, J.-M., Platevoët, B., et al. (2011). Segregation of olivine grains in volcanic sands in Iceland and implications for Mars. *Earth and Planetary Science Letters*, *310*(3–4), 233–243. https://doi.org/10.1016/j.epsl.2011.07.025

Mangold, N., Quantin, C., Ansan, V., Delacourt, C., & Allemand, P. (2004). Evidence for precipitation on Mars from dendritic valleys in the Valles Marineris area. *Science*, *305*, 78–81. https://doi.org/10.1126/science.1097549

Márquez, A., de Pablo, M. A., Oyarzun, R., & Viedma, C. (2005). Evidence of gully formation by regional groundwater flow in the Gorgonum–Newton region (Mars). *Icarus*, *179*(2), 398–414. https://doi.org/10.1016/j.icarus.2005.07.020

McEwen, A. S., Eliason, E. M., Bergstrom, J. W., Bridges, N. T., Hansen, C. J., Delamere, W. A., et al. (2007). Mars reconnaissance orbiter's high resolution imaging science experiment (HiRISE). *Journal of Geophysical Research*, *112*, E05S02. https://doi.org/10.1029/2005JE002605
McGuire, P. C., Bishop, J. L., Brown, A. J., Fraeman, A. A., Marzo, G. A., et al. (2009). An improvement to the volcano-scan algorithm for atmospheric correction of CRISM and OMEGA spectral data. *Planetary and Space Science*, *7*(7), 809–815. https://doi.org/10.1016/j.pss.2009.03.007
Mellon, M. T., Jakosky, B. M., Kieffer, H. H., & Christensen, P. R. (2000). High-resolution thermal inertia mapping from the Mars global surveyor thermal emission spectrometer. *Icarus*, *148*(2), 437–455. https://doi.org/10.1006/icar.2000.6503
Michael, G. G., & Neukum, G. (2010). Planetary surface dating from crater size-frequency distribution measurements: Partial resurfacing events and statistical age uncertainty. *Earth and Planetary Science Letters*, *294*, 223–229. https://doi.org/10.1016/j.epsl.2009.12.041
Michael, G. G., Platz, T., Kneissl, T., & Schmedeman, N. (2012). Planetary surface dating from crater size frequency distribution measurements: Spatial randomness and clustering. *Icarus*, *218*(1), 169–177. https://doi.org/10.1016/j.icarus.2011.11.033
Michalski, J., Dobrea, E., Niles, P., & Cuadros, J. (2017). Ancient hydrothermal seafloor deposits in Eridania basin on Mars. *Nature Communications*, *8*, 15978. https://doi.org/10.1038/ncomms15978
Michalski, J., & Niles, P. B. (2012). Atmospheric origin of Martian layered deposits: Links to climate change and the global sulfur cycle. *Geology*, *40*(5), 419–422. https://doi.org/10.1130/G32971.1
Mueller, K., & Golombek, M. P. (2004). Compressional structures on Mars. *Annual Review of Earth and Planetary Sciences*, *32*, 435–464. https://doi.org/10.1146/annurev.earth.32.101802.120553
Murchie, S., Arvidson, R., Bedini, P., Beisser, K., Bibring, J.-P., Bishop, J., et al. (2007). Compact reconnaissance imaging spectrometer for Mars (CRISM) on Mars reconnaissance orbiter (MRO). *Journal of Geophysical Research*, *112*, E05S03. https://doi.org/10.1029/2006JE002682
Mustard, J. F., Cooper, C. D., & Rifkin, M. K. (2001). Evidence for recent climate change on Mars from the identification of youthful near-surface ground ice. *Nature*, *412*, 411–414. https://doi.org/10.1038/35086515
Osterloo, M. M., Anderson, F. S., Hamilton, V. E., & Hynek, B. M. (2010). Geologic context of proposed chloride-bearing materials on Mars. *Journal of Geophysical Research*, *115*, E10012. https://doi.org/10.1029/2010JE003613
Osterloo, M. M., Hamilton, V. E., Bandfield, J. L., Glotch, T. D., Baldridge, A. M., Christensen, P. R., et al. (2008). Chloride-bearing materials in the southern highlands of Mars. *Science*, *319*, 1651–1654. https://doi.org/10.1126/science.1150690
Pain, C. P., Clarke, J. D. A., & Thomas, M. (2007). Inversion of relief on Mars. *Icarus*, *190*, 478–491. https://doi.org/10.1016/j.icarus.2007.03.017
Pajola, M., Rossato, S., Carter, J., Baratti, E., Pozzobon, R., Erculiani, M. S., et al. (2016). Eridania Basin: An ancient paleolake floor as the next landing site for the Mars 2020 rover. *Icarus*, *275*, 163–182. https://doi.org/10.1016/j.icarus.2016.03.029
Palumbo, A. M., Head, J. W., & Wordsworth, R. D. (2018). Late Noachian Icy Highlands climate model: Exploring the possibility of transient melting and fluvial/lacustrine activity through peak annual and seasonal temperatures. *Icarus*, *300*, 261–286. https://doi.org/10.1016/j.icarus.2017.09.007
Pan, C., Rogers, A. D., & Michalski, J. R. (2015). Thermal and near-infrared analyses of central peaks of Martian impact craters: Evidence for a heterogeneous Martian crust. *Journal of Geophysical Research: Planets*, *120*, 662–688. https://doi.org/10.1002/2014JE004676
Papike, J. J., Karner, J. M., & Shearer, C. K. (2006). Comparative planetary mineralogy: Implications of martian and terrestrial jarosite. A crystal chemical perspective. *Geochimica et Cosmochimica Acta*, *70*, 1309–1321. https://doi.org/10.1016/j.gca.2005.11.004
Pascuzzo, A. C., Mustard, J. F., Kremer, C. H., & Ebinger, E. (2019). The formation of irregular polygonal ridge networks, Nili Fossae, Mars: Implications for extensive subsurface channelized fluid flow in the Noachian. *Icarus*, *319*, 852–868. https://doi.org/10.1016/j.icarus.2018.10.020
Pelkey, S. M., Jakosky, B. M., & Christensen, P. R. (2003). Surficial properties in Melas Chasma, Mars, from Mars Odyssey THEMIS data. *Icarus*, *165*(1), 68–89. https://doi.org/10.1016/S0019-1035(03)00152-0
Peretyazhko, T. S., Niles, P. B., Sutter, B., Morris, R. V., Agresti, D. G., Le, L., & Ming, D. W. (2017). Smectite formation in the presence of sulfuric acid: Implications for acidic smectite formation on early Mars. *Geochimica et Cosmochimica Acta*, *220*, 248–260. https://doi.org/10.1016/j.gca.2017.10.004
Presley, M. A., & Christensen, P. R. (1997). The effect of bulk density and particle size sorting on the thermal conductivity of particulate materials under Martian atmospheric pressures. *Journal of Geophysical Research*, *102*(E4), 9221–9230. https://doi.org/10.1029/97JE00271
Pye, K., & Tsoar, H. (2009). *Mechanics of Aeolian Sand Transport. Aeolian sand and sand dunes*. Berlin, Heidelberg: Springer. https://doi.org/10.1007/978-3-540-85910-9_4
Schultz, R. A. (2000). Localization of bedding plane slip and backthrust faults above blind thrust faults: Keys to wrinkle ridge structure. *Journal of Geophysical Research*, *105*, 12035–12052. https://doi.org/10.1029/1999je001212
Silvestro, S., Pacifici, A., Salese, F., Vaz, D. A., Neesemann, A., Tirsch, D., et al. (2021). Periodic bedrock ridges at the ExoMars 2022 landing site: Evidence for a changing wind regime. *Geophysical Research Letters*, *48*(4), e2020GL091651. https://doi.org/10.1029/2020GL091651
Skinner, J. A., Fortezzo, C. M., & Mouginis-Mark, P. J. (2021). Exposure of an early to middle Noachian valley network in three dimensions on Mars. *Icarus*, *354*, 114071. https://doi.org/10.1016/j.icarus.2020.114071
Smith, D. E., Zuber, M. T., Frey, H. V., Garvin, J. B., Head, J. M., Muhleman, D. O., et al. (2001). Mars orbiter laser altimeter: Experiment summary after the first year of global mapping of Mars. *Journal of Geophysical Research*, *106*, 23689–23722. https://doi.org/10.1029/2000JE001364
Viviano-Beck, C. E., Seelos, F. P., Murchie, S. L., Kahn, E. G., Seelos, K. D., Taylor, H. W., et al. (2014). Revised CRISM spectral parameters and summary products based on the currently detected mineral diversity on Mars. *Journal of Geophysical Research: Planets*, *119*, 1403–1431. https://doi.org/10.1002/2014JE004627
Warner, N. H., Grant, J. A., Wilson, S. A., Golombek, M. P., DeMott, A., Charalambous, C., et al. (2020). An impact crater origin for the InSight landing site at Homestead hollow, Mars: Implications for near surface stratigraphy, surface processes, and erosion rates. *Journal of Geophysical Research: Planets*, *125*, e2019JE006333. https://doi.org/10.1029/2019JE006333
Wendt, L., Bishop, J. L., & Neukum, G. (2013). Knob fields in the Terra Cimmeria/Terra Sirenum region of Mars: Stratigraphy, mineralogy and morphology. *Icarus*, *225*, 200–215. https://doi.org/10.1016/j.icarus.2013.03.020
Werner, S. C., & Tanaka, K. L. (2011). Redefinition of the crater-density and absolute-age boundaries for the chronostratigraphic system of Mars. *Icarus*, *215*(2), 603–607. https://doi.org/10.1016/j.icarus.2011.07.024
Williams, R. M. E., Moersch, J. E., & Fergason, R. L. (2018). Thermophysical properties of Martian fluvial sinuous ridges: Inferences on "inverted channel" induration agent. *Earth and Space Science*, *5*, 516–528. https://doi.org/10.1029/2018EA000402
Willmes, M., Reiss, D., Hiesinger, H., & Zanetti, M. (2012). Surface age of the ice–dust mantle deposit in Malea Planum, Mars. *Planetary and Space Science*, *60*(1), 199–206. https://doi.org/10.1016/j.pss.2011.08.006

Wilson, L., & Head, J. W., III (2002). Tharsis-radial graben systems as the surface manifestation of plume-related dike intrusion complexes: Models and implications. *Journal of Geophysical Research*, *107*(E8), 5057. https://doi.org/10.1029/2001JE001593

Wordsworth, R., Forget, F., Millour, E., Head, J. W., Madeleine, J.-B., & Charnay, B. (2013). Global modelling of the early Martian climate under a denser CO_2 atmosphere: Water cycle and ice evolution. *Icarus*, *222*, 1–19. https://doi.org/10.1016/j.icarus.2012.09.036

Wordsworth, R. D. (2016). The climate of early Mars. *Annual Review of Earth and Planetary Sciences*, *44*, 381–408. https://doi.org/10.1146/annurev-earth-060115-012355

Wray, J. J., Milliken, R. E., Dundas, C. M., Swayze, G. A., Andrews-Hanna, J. C., et al. (2011). Columbus crater and other possible groundwater-fed paleolakes of Terra Sirenum, Mars. *Journal of Geophysical Research*, *116*, E01001. https://doi.org/10.1029/2010JE003694